Journal of Geophysical Research: Atmospheres

RESEARCH ARTICLE
10.1029/2018JD028965

The Great Slave Lake PyroCb of 5 August 2014: Observations, Simulations, Comparisons With Regular Convection, and Impact on UTLS Water Vapor

G. KablickIII[1,2], M. Fromm[1], S. Miller[3], P. Partain[3], D. Peterson[4], S. Lee[2], Y. Zhang[2], A. Lambert[5], and Z. Li[2]

[1]US Naval Research Laboratory, Washington, DC, USA, [2]Department of Atmospheric and Oceanic Science, University of Maryland, College Park, MD, USA, [3]Colorado State University, Cooperative Institute for Research in the Atmosphere, Fort Collins, CO, USA, [4]US Naval Research Laboratory, Monterey, CA, USA, [5]Jet Propulsion Laboratory, California Institute of Technology, Pasadena, CA, USA

Key Points:
- Observations and simulations of a pyroCb show a distinct convective lifecycle from meteorological Cb
- A-Train observations show ice sublimation in the aging plume over five days and enhanced localized water vapor in the stratosphere
- Model tests show pyroCb dynamics is dominated by surface heat flux, with lesser dependence on aerosol loading and midlevel instability.

Supporting Information:
- Supporting Information S1
- Movie S1
- Movie S2

Correspondence to:
G. P. Kablick III,
george.kablick@nrl.navy.mil

Citation:
Kablick, G. P., Fromm, M. D., Miller, S. D., Partain, P., Peterson, D., Lee, S. S., et al. (2018). The Great Slave Lake pyroCb of 5 August 2014: Observations, simulations, comparisons with regular convection, and impact on UTLS water vapor. *Journal of Geophysical Research: Atmospheres*, *123*. https://doi.org/10.1029/2018JD028965

Received 7 MAY 2018
Accepted 24 SEP 2018
Accepted article online 23 OCT 2018

Abstract This study analyzes a pyrocumulonimbus (pyroCb) that formed near Great Slave Lake in the Northwest Territories of Canada on 5 August 2014 using multiple satellite- and ground-based data sets, meteorological reanalysis, and a cloud-resolving model. Passive and active polar-orbiting instruments and geostationary imagery detail the intense updraft column during the several hours-long convective stage and capture the entire pyroCb life cycle. CloudSat radar reflectivity profiles and local soundings show the pyroCb cloud base was ≥1 km above the lifting condensation level. Comparisons with profiles through meteorological convection in the same region reaffirm previous evidence for delayed droplet growth within pyroconvective updrafts. The pyroCb penetrated the tropopause, reaching at least 14 km ($\theta \simeq 380$ K), and the detrained cirrus/smoke plume was tracked over the following 2 weeks using lagrangian trajectories, the Cloud-Aerosol Lidar with Orthogonal Polarization and Microwave Limb Sounder. Microwave Limb Sounder ice water content and water vapor mixing ratio (WVMR) observations in the aging plume show ice sublimation occurred in the stratosphere, producing individual WVMR anomalies up to +5 ppmv and plume-averaged anomalies up to +2 ppmv. Reanalysis indicates the pyroCb formed in favorable convective conditions, but we show the fire itself triggered convection because meteorological triggers were not colocated during initiation. Cloud-resolving model simulations confirm this result when controlled for surface fluxes, initial thermodynamics, and aerosol loading. Sensitivity tests show surface heat flux is dominant in determining overall pyroCb intensity, but aerosols and moisture inflow can effect small changes in updraft velocity, anvil ice concentration, and detrained WVMR.

1. Introduction

Pyrocumulonimbus (pyroCb) events have been established as a regular phenomenon in the boreal summer that routinely penetrate the tropopause (Damoah et al., 2006; Fromm et al., 2010; Peterson, Fromm, et al., 2017). They typically form over large wildland fires in the middle to high latitudes on an annual basis and produce a plume composed of a mixture of biomass-burning aerosols, gases, and cloud ice particles that otherwise would not be present in the upper troposphere/lower stratosphere (UTLS) in such abundance (Fromm & Servranckx, 2003). Since their discovery, scientific understanding of these events has increased: a conceptual model has been put forth regarding the meteorological and burning conditions necessary for pyroCb development (hereafter *P*17b; Peterson, Hyer, et al., 2017); the droplet and ice particle size distributions (PSD) have been shown to possess a very small effective radius (Rosenfeld et al., 2007); and the outflow anvils are known to have a distinct increase in lifetime compared with meteorological cumulonimbus (Cb) forming in the same synoptic conditions(hereafter *L*08; Lindsey & Fromm, 2008). However, there are still several aspects of the pyroCb phenomenon that require a better understanding, such as the internal dynamics of the updraft column, the relative importance of aerosol-cloud microphysical interactions, and the stratospheric impact of an injected ice/smoke plume. Here we present a study exploring these aspects.

Both observations and modeling studies of regular (non-pyro-) convection have shown that small ice particles result from an increase in aerosol in the boundary layer (Fan et al., 2013; Khain et al., 2005; Rosenfeld et al., 2008). In these situations the cloud condensation nuclei (CCN) abundance reduces the average droplet

size in the updraft columns, and a so-called *invigoration effect* may result (Rosenfeld et al., 2008). A reduction in droplet size limits collisions and coalescence, thereby maintaining a greater amount of condensed water that will increase latent heating above the freezing level (FL) and enhance the buoyancy of rising air (Khain et al., 2005; Rosenfeld & Woodley, 2000). For pyroCb events, idealized model simulations have also shown that a large CCN concentration can significantly enhance latent heat release (Reutter et al., 2014), but the role of this aerosol effect on updraft velocity was shown to be small when compared with buoyancy enhancements from extreme sensible heat fluxes over a fire (Luderer et al., 2006). An additional consideration behind the large number density of small ice particles in convective clouds is the strength of the updraft itself. The supersaturations are larger in such conditions, leading to rapid generation of ice crystals above the FL (Rosenfeld et al., 2007). Regardless of the dominant influence—whether it is a CCN effect on the PSD or the surface heat flux—it is certain that pyroconvection has intense updrafts and clouds with very small droplets and ice crystals.

A corollary to diminishing ice crystal size is that the inefficient removal of these particles has the potential to increase absolute humidity within an aging plume. Ice particles that comprise convective anvils undergo various removal processes as they age, including sublimation and sedimentation. Sublimation occurs when conditions become subsaturated with respect to ice as the anvil mixes with ambient air. In a study based on convective anvil penetration of the tropical tropopause, Sherwood (2002b) hypothesized that mixing drier air into ice-rich cirrus containing small particles would reduce the saturation ratio to the point that ice sublimation would increase downstream absolute humidity as compared with cirrus with larger particles. A follow-up paper was published by the same author, and relied on geostationary satellites to infer there was a detectable anticorrelation between tropical UTLS absolute humidity and convective anvil ice particle size (Sherwood, 2002a). In other words, smaller effective radii in convective cirrus near the tropical tropopause preceded an increase in water vapor concentrations at higher altitudes, to where tropical upper tropospheric air slowly migrates (Fueglistaler et al., 2009). However, cross-tropopause transport in the middle to high latitudes is comparatively rare and is typically only a result of direct injection (Bedka, 2011; Holton et al., 1995). It remains unknown whether a pyroCb has the potential to moisten the air in the midlatitude UTLS as a result of small ice particle/sublimation effects.

Another process to consider is sedimentation, which could reduce the impact a sublimating ice cloud would have on absolute humidity by removing a potential vapor source from the parcel. In this process ice precipitates to lower altitudes after the updrafts maintaining the suspended particles are weakened or as particles aggregate into sizes large enough to gravitationally overcome the updraft forces. In their study on tropical convective anvils, Jensen et al. (2009) noted that both the sublimation and growth rates of ice crystals are a function of the saturation ratio and a deposition coefficient (see their Figure 11). They used in situ aircraft observations during the Tropical Composition, Cloud, and Climate Coupling campaign to argue that small ice crystals do not persist longer than a few hours; they either grow through deposition or they completely sublimate in subsaturated air; their results were consistent with previous work on other types of small-ice-crystal clouds such as wave clouds. In the case of a pyroCb, an anvil would need to have an ice saturation ratio very close to 1.0 in order for the crystals to neither sublimate nor grow too quickly to be removed by sedimentation. *L*08 used infrared observations to show pyroCb anvils persisted between ~18 and 30 hr longer than that of nearby meteorological Cb anvils postdetrainment, which would mean the saturation ratio must be favorable to ice for a longer period of time.

In addition to aerosols and ice, pyroCb are known to inject a large amount of combustion-generated gases into the stratosphere (Pumphrey et al., 2011). One of these is water vapor, which has the distinct role of contributing to hydrometeor and latent heat processes throughout the depth of the convective cloud (Potter, 2005). Meteorological deep convection over North America and the Asian Monsoon is known to inject locally substantial amounts of water vapor into the lower-most stratosphere, but the net effect of those injections is thought to be small (Schwartz et al., 2013). PyroCb, however, are unusually intense and their cloud properties are distinct from Cb, so an important question is whether ice microphysics plays a role in the amount of water vapor injected into the LS during these events since changes to ice PSD may affect changes in sublimated vapor downstream. For this to be true, ice crystals would have to sublimate in the UTLS instead of being removed through sedimentation. The best way to address this question would be from in situ aircraft measurements through active and detrained pyroCb anvils. Unfortunately such an encounter has not been documented, so in this study we rely on remote sensing instruments and a cloud-resolving model.

We analyze the life cycle of a pyroCb that formed south of Great Slave Lake (GSL) in the Northwest Territories of Canada. The pyroCb (hereafter GSL pyroCb) began at approximately 18:45 UTC on 5 August 2014 over fire 14WB-025 (number designation used by Parks Canada/Wood Buffalo National Park; 60.2°N, 115.5°W). The fire had been burning for approximately 6 days after a lightning strike on 30 July. There were many fires burning in and around the Wood Buffalo National Forest and GSL regions at the time, some of which had already produced pyroCbs prior to 5 August, but the GSL pyroCb had fortuitous satellite coverage in addition to several ground stations recording observations nearby during the active stages of convection. Additionally, the detrained plume was observable by instruments in NASA's A-Train for over 2 weeks after the event. As such it provides a useful case for an examination of a complete pyroCb lifecycle, including any water vapor impact of UTLS-injected ice. The objectives of this study are fourfold: in section 2 we (i) establish a timeline of the GSL pyroCb event, focusing on the fire, meteorological conditions, and infrared cloud properties and (ii) differentiate between the active pyroCb and contemporaneous Cb using CloudSat reflectivity profiles, discussing the differences in anvil lifetime; in section 3 we (iii) quantify the pyroCb plume's localized impact on stratospheric water vapor; and in section 4 we (iv) use cloud-resolving simulations to estimate the sensitivity of pyroCb development and detrained absolute humidity to environmental variables.

2. Active Convective Stage

Over the course of three hours on 5 August, multiple polar-orbiting satellites captured the growth and development of the GSL pyroCb prior to, during, and after the active stages of convection. Figure 1 shows True-Color images by the MODerate Imaging Spectroradiometer (MODIS) from both the Aqua (Figures 1a and 1e) and Terra (Figures 1b and 1d) platforms and similar images by the Visible Imaging Infrared Radiometer Suite (VIIRS) on-board Suomi NPP (Figures 1c and 1f). A combination of the high northern latitude summertime conditions and the unusually early local time for pyroconvection (12:45 local time) allowed each of these imagers to capture multiple daytime passes. The six snapshots in Figure 1 show the GSL fire near the center of the images, and document the pyroCb from the early stages of cumulus congestus (Figures 1a–1c) through the mature convective column (Figures 1d and 1e) and the detraining anvil stage (Figure 1f). At approximately 20:20 UTC (14:20 local time), Aqua MODIS made its second daytime pass (Figure 1e), which occurred directly over the pyroCb column. The red line in Figure 1e shows the nadir ground track of the active A-Train instruments discussed later in this section: the CloudSat Profiling Radar (CPR, Stephens et al., 2002) and the Cloud-Aerosol Lidar with Orthogonal Polarization (CALIOP, Winker et al., 2009).

In the days leading up to the GSL pyroCb, there was a large amount of smoke being generated in the region, and it prevented many of the perimeter flights used to accurately estimate daily fire progression (personal communication with Northwest Territory Fire Resource personnel). However, perimeter data derived from MODIS Level 2 hot spots indicate the fire consumed about 65,400 ha in total during the 6-day period between ignition and the pyroCb event. The fire just to the east of center in Figure 1 at ~114°W (fire 14WB-028; hereafter *Eastern Fire*) also produced a pyroCb. Cumulus congestus is also seen forming and dissipating over the Eastern Fire throughout the six snapshots in Figure 1, but it does not develop a pyroCb until after the anvil from the GSL pyroCb passes nearby, at which time it became apparent in geostationary imagery (see supporting information Movies S1 and S2 for thermal infrared and visible GOES-15 animations of these events). The intense convection from the Eastern Fire did not produce a mature pyroCb until approximately 22:30 UTC, 2 hr after the GSL Fire. It is likely that the anvil from the Eastern Fire pyroCb interacted with the GSL pyroCb anvil blowoff to produce a larger UTLS plume than would have existed otherwise as indicated by the two-tiered appearance of the early morning visible-band *day after* plume at 11:30 UTC on 6 August (Movie S2). It is unknown why the two pyroCbs, both within the same region favorable to convection (discussed in section 2.1), developed over 2 hr apart. Any number of factors such as fuel types and microscale meteorology could play a role in different rates of development for two pyroCb in the same region, but an in depth examination of the sensitivity to these variables is beyond the scope of this work. However, the time delay between the onset of each pyroCb is an indication that the fire, not the environment, is the trigger. In section 2.1 we analyze the meteorological state and discuss other possible triggers for convection, and in section 4 we show using model simulations that the surface heat flux is likely the most important factor in determining pyroCb generation.

Figure 2 contains VIIRS brightness temperatures at 3.7 μm (BT_3) during the times corresponding to Figures 1c and 1f. The images are constructed so the fire location hot spots identified by this channel are displayed as red-orange-yellow colors with the GSL Fire denoted by the yellow arrow, and the cooler BT_3 values corresponding to terrestrial and cloud temperatures are in gray-scale. One common feature observed with pyroCbs

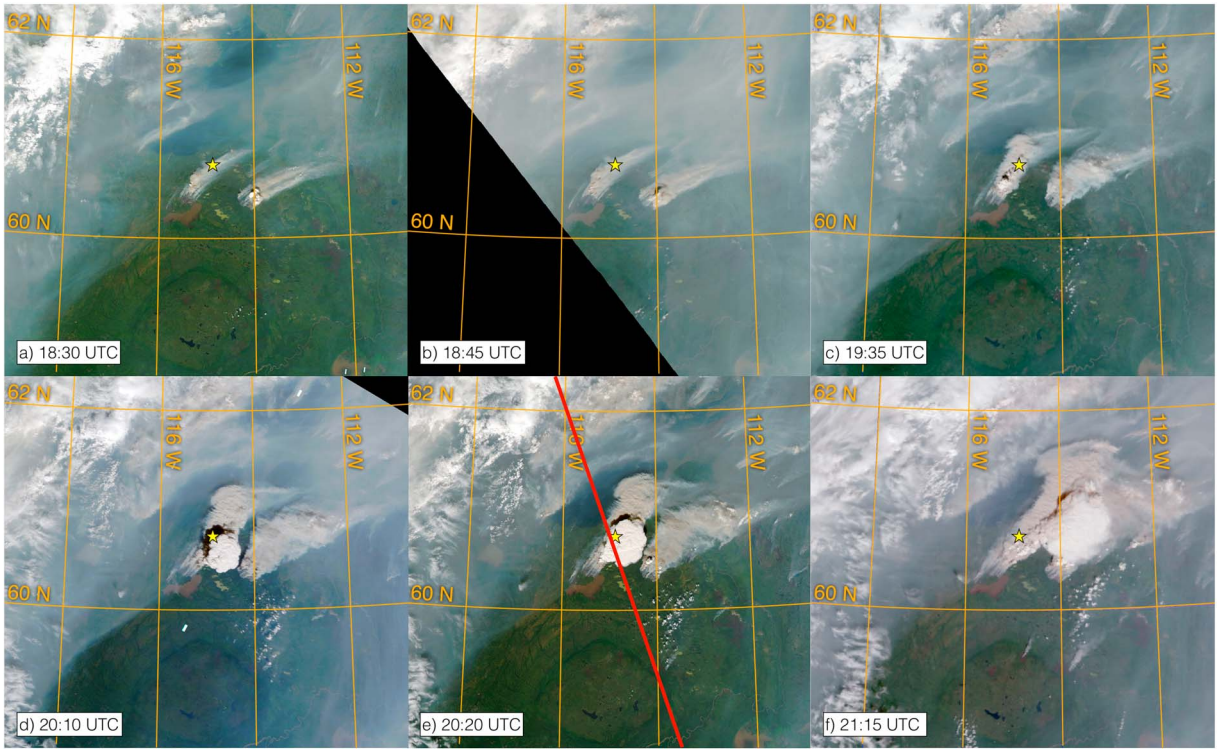

Figure 1. Visible imagery of the Great Slave Lake pyrocumulonimbus over the course of 3 hr on 5 August as seen by Aqua Moderate Imaging Spectroradiometer (a, e), Terra Moderate Imaging Spectroradiometer (b, d), and NPP Visible Imaging Infrared Radiometer Suite (c, f). The yellow star indicates the location of the Buffalo Junction ground observation site, across which the active pyroCb moved. The red line in (e) shows the nadir ground track of Cloud-Aerosol Lidar with Orthogonal Polarization and CloudSat during the mature convective stage. The changes in apparent brightness of smoke and haze between each image are due to the increase/decrease in sunlight scattering into the sensor as the viewing angle changes.

in this part of the BT spectrum is a *warm* anvil (*L*08, Fromm et al., 2010). Lindsey et al. (2006) explained there is a strong inverse relationship between daytime BT_3 and ice particle size for diameters <80 μm at a constant solar zenith angle since the solar reflectance component increases dramatically with decreasing effective radius (r_e). In the terrestrial-only infrared part of the spectrum (e.g., channels such as 11 and 12 μm), there is an insignificant contribution from solar reflectance, and for optically thick clouds at a given emitting temperature there is little difference in behavior of these BTs with particle size. The largest influence in these channels is the temperature of the cloud itself. A visual comparison of the pyroCb anvil BT_3 in Figure 2b (yellow circle) to that of the cirrus clouds in the upper left corner of the images highlight the effect of particle size.

However, the optical thickness of a cloud needs to be accounted for when assuming daytime BT_3 *warmness* indicates a small r_e. BT from pixels containing semitransparent clouds, for example, can have a significant contribution of radiance from emission below the cloud layer, making them appear warmer than opaque clouds at the same altitude. Figure 2c shows the BT_{11} from VIIRS for the same scene as in Figure 2b, and Figure 3a shows the same channel from Aqua MODIS at 20:20 UTC (corresponding with Figure 1c). Minimum BT_{11} for the pyroCb top is −62 °C, and the anvil has a distinct *cold-U* feature sometimes seen with intense, overshooting thunderstorms that can have the central updraft reach warmer levels in the lower stratosphere (Setvák et al., 2010). One commonly used cloud optical opacity test is the brightness temperature difference between two thermal infrared channels in the atmospheric window, in this case MODIS channels 32 (12 μm) and 31 (11 μm), denoted herein as BTD_{12-11}. Small absolute values ($|BTD_{12-11}|$<3.0 °C) indicate optically thick clouds. This test was validated by Peterson, Fromm, et al. (2017) for use with pyroCb anvils, and the result of that test on the GSL pyroCb anvil yields a BTD_{12-11} spread between −0.1 and +1.0 °C; well within the *optically thick* range. This result gives confidence that the warm daytime BT_3 values indicate an abundance of very small ice particles in the anvil. There can be a solar zenith angle effect on BT_3 due to scattering, but when this angle is small it is usually limited to the edges of clouds. This effect can be seen in Figure 2b: the anvil BT_3 is quite warm on the south-facing fringe and cloud top, and much colder toward the north where the anvil slopes away from solar illumination.

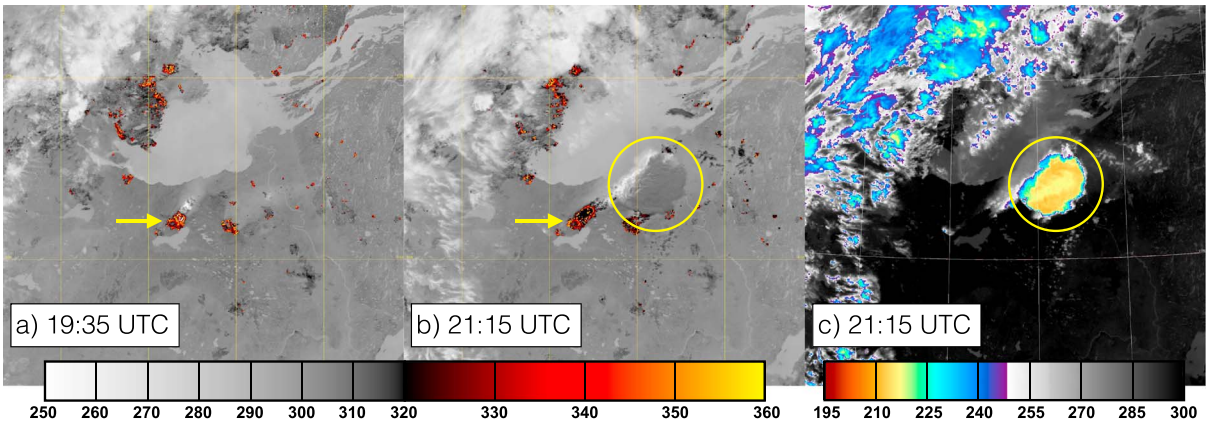

Figure 2. As in Figure 1c and 1f, but for Visible Imaging Infrared Radiometer Suite 3.7 μm (a, b) and 10.8 μm (c) Brightness Temperatures. All values are in K. Images (b) and (c) are ~100 min after (a) on 5 August. Fire 14WB-025 is denoted with yellow arrow in (a) and (b). Note the darker color of the pyroCb anvil (yellow circle) in (b) as compared with the lighter cirrus clouds to the northwest (upper left of images) as the convection becomes detached from the fire, indicating an extremely small and narrow ice particle size distribution.

A few minutes earlier during the same daytime Aqua MODIS pass, the A-Train observed a concurrent meteorological Cb in central Alberta (Figure 3b; hereafter Alberta Cb) centered at 53.5°N. The Alberta Cb underwent convective development at approximately the same time (~ 12:45 local time) as the GSL pyroCb as seen in GOES-West (GOES-15) imagery and had a minimum BT_{11} = −64 °C with $|BTD_{12-11}|$ <1.0 °C, and a more uniform appearance to the BT field (no cold-U). CloudSat and CALIOP also passed directly over a deep convective portion of the Alberta Cb, as shown by a red line. Figure 4 contains the curtains through both the GSL pyroCb and the Alberta Cb from these sensors. Level 1 CALIOP 532 nm total attenuated backscatter (β'_{532}) is shown above the corresponding CloudSat CPR 94 GHz radar reflectivity from the 2B-GEOPROF product, and overlaid on the images is a dashed line that represents the uppermost cloud observation by CALIOP for each case.

The lidar detects the pyroCb overshooting cloud top altitude to be approximately 14 km above mean sea level (a.m.s.l.), whereas the radar does not observe this overshoot. It has a maximum cloud height detection of 13 km (Figures 4a and 4c). CALIOP observes large β'_{532} and full attenuation within a very narrow vertical depth (<1 km), whereas the CPR has radar reflectivities beneath the noise threshold of −28 dBZ_e at these uppermost cloud top levels. This discrepancy is not present with the Cb case, where both instruments detect a cloud near 12 km (Figures 4b and 4d). The sensitivities of these instruments to ice particle size have been documented in

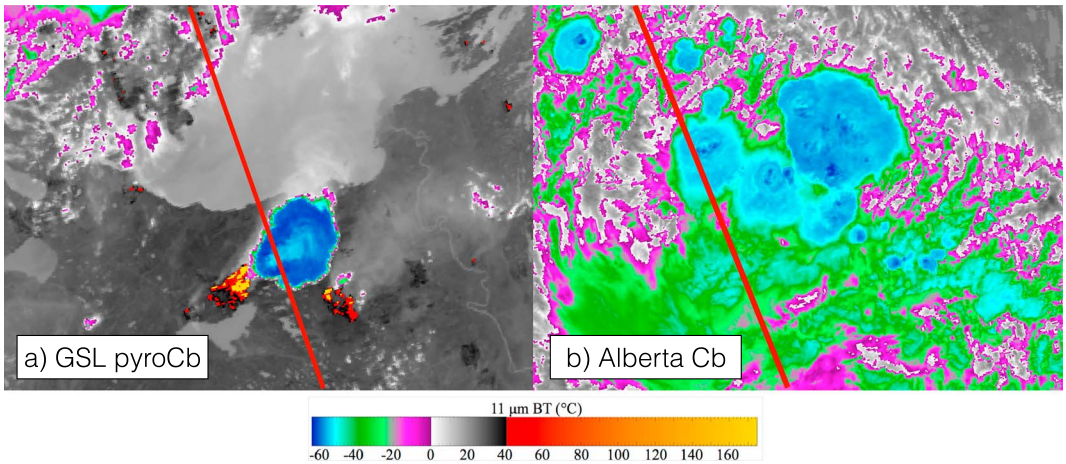

Figure 3. Aqua Moderate Imaging Spectroradiometer BT_{11} of the GSL pyroCb (a) and the concurrent Alberta Cb to the south (b) at 20:20 UTC. The red lines show the nadir ground track of Cloud-Aerosol Lidar with Orthogonal Polarization and CloudSat. Note the *cold-U* shape of the pyroCb outflow anvil with warmer temperatures corresponding to the central overshooting top. The Cb shows no such structure even though the minimum brightness temperatures are similar: −62 and −64 °C for pyroCb and Cb, respectively. GSL = Great Slave Lake; pyroCb = pyrocumulonimbus.

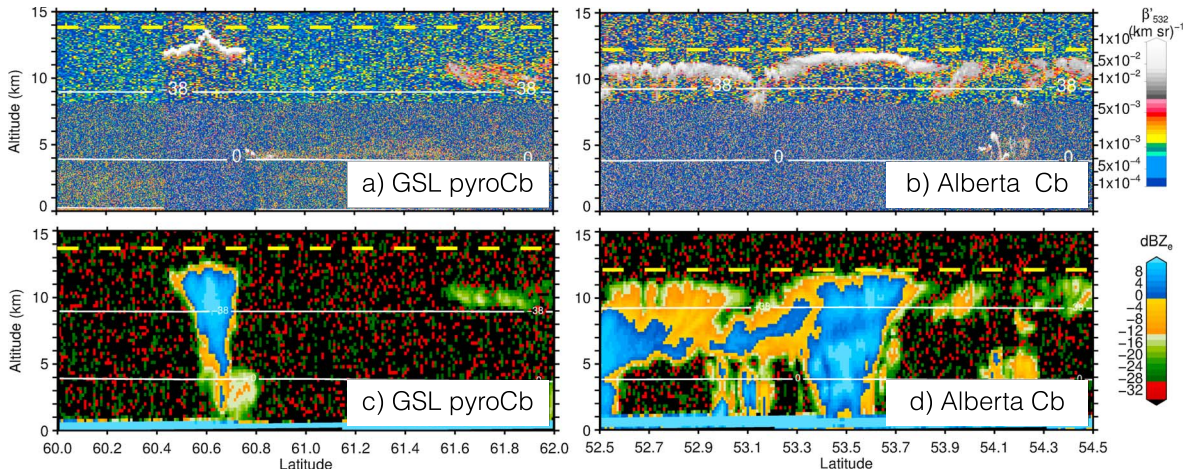

Figure 4. CALIOP 532 nm backscatter (top row) and CloudSat 94 GHz radar reflectivity (bottom row) at the 20:20 UTC intersection of the active GSL pyroCb (a,c) and Alberta Cb (b,d) cores (see red line in Figures 1e and 2a for pyroCb and Figure 2b for Cb). CALIOP shows that the GSL pyroCb has a highly attenuating anvil cloud with overshooting top near 14 km (a), and CloudSat indicates strong echoes in the midlevels, but weak echoes near the surface, and no echoes between 13 and 14 km (c). The yellow dashed line indicates the CALIOP cloud top in both panels. Conversely for the Alberta Cb, CALIOP (b) and CloudSat (d) have similar cloud top heights, and the radar reflectivity shows a complex vertical structure of with large reflectivity near the cloud top and extending down to the surface. Also shown are the 0 and −38 °C isotherms from ERA-I reanalysis at both locations. GSL = Great Slave Lake; pyroCb = pyrocumulonimbus; CALIOP = Cloud-Aerosol Lidar with Orthogonal Polarization.

many places (Austin et al., 2009; Delanoë & Hogan, 2010; Miller & Stephens, 2001; Stephens et al., 2002) and is thought to be the cause of the cloud top discrepancy in the GSL pyroCb. The midvisible CALIOP is most sensitive to the second moment of a PSD—proportional to the total cross-sectional area of all particles contributing to scattering—whereas the W-Band CPR is most sensitive to the sixth moment—proportional to the total volume of scatterers. Therefore, the GSL pyroCb anvil must be composed of a large number of very small scatterers as compared with the Alberta Cb. Using this reasoning in combination with the warm BT_3 and cold BT_{11} (Figures 2 and 3, respectively) we conclude that the GSL pyroCb generated an extremely narrow ice PSD with very small r_e. Note that these two instruments orbit in a formation designed to observe the same scene—nominally flying within 15 s of each other—so differences in cloud morphology between observations is minimal and would not account for the apparent cloud top discrepancy. The different sensitivities of CALIOP and CPR to cloud top particle size is documented in many places (Miller et al., 2001; Weisz et al., 2007), and recent exploitation of this difference has produced new understanding about how aerosols can affect ice particles near the cloud top (Caffrey et al., 2018; Fromm et al., 2016).

An interesting feature of note in Figure 4c is the large value of radar reflectivity associated with apparently dry smoke just to the northwest of the pyroCb. This smoke is visible below ~4 km between 60.7 and 60.8°N (compare with MODIS image in Figure 1e) and has values approaching −5 dBZ_e. Lofted smoke is typically not detected directly by the 94 GHz CloudSat radar because by the time an observation is made, the plume has aged to the point where the only remaining particles are those produced chemically through combustion (which are less than 1 μm in diameter) and would not be sensed at this frequency. However, this plume being close to the source likely contains biomass-burning debris with a relatively large radar cross section that has not yet fallen out (Fromm et al., 2012). The size distributions of aerosols in smoke plumes are known to depend on, among other things, fire kinetic temperature and oxygen availability (Reid et al., 2005), and radar studies have shown effects on reflectivity depending on the composition and age of smoke plume and the radar frequency (Banta et al., 1992; Jones & Christopher, 2010; Melnikov et al., 2009). It is likely this pyroconvection smoke contains a substantial amount of CCN, but it is unlikely that debris large enough to produce radar reflectivities in CloudSat would participate in cloud particle formation. This topic is discussed further in section 4.

Plotted on top of each panel in Figure 4 are the isotherms at $T = 0$ and −38 °C from the CloudSat ECMWF-AUX product—the FL and homogeneous FL (HFL), respectively. These thermodynamic levels are known to be important boundaries for latent heat processes in convection, so they are denoted on these curtains for later reference. In section 2.2 we use these thermodynamic boundaries in addition to the lifting condensation level (LCL) and equilibrium level (EL) to discuss the microphysical interpretation of the CPR reflectivity profiles of

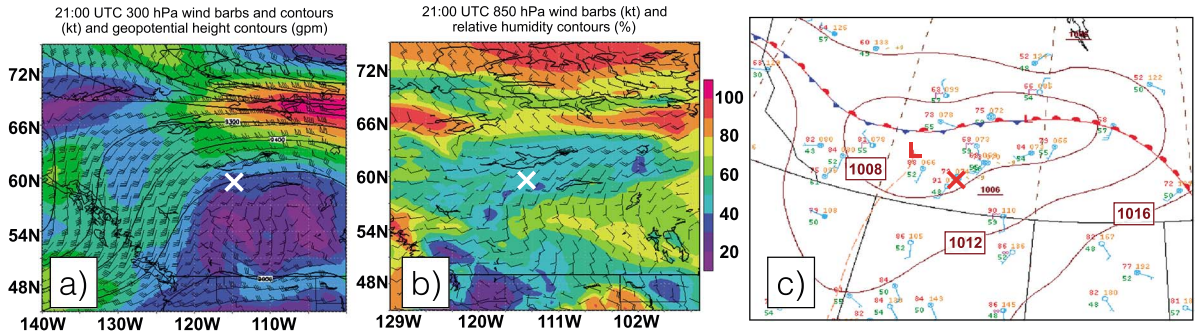

Figure 5. Synoptic-scale conditions from North American Regional Reanalysis showing winds and geopotential heights at 300 hPa (a), relative humidity and winds at 850 hPa (b), and surface frontal analysis (c). "×" symbols denote location of pyroCb.

the GSL pyroCb and Alberta Cb. We also include a statistical analysis of additional CPR intercepts through the cores of deep convection clouds from the same region and season. Prior to that discussion, however, it is useful to establish the meteorology and fire precursors.

2.1. Weather and Fire Conditions

Figure 5 shows the weather conditions in place prior to the initiation of convection. Winds and geopotential heights at 300 hPa from the North American Regional Reanalysis (Mesinger et al., 2006) indicate the pyroCb formed at the southern edge of a jet entrance-region with an approaching shortwave trough aligned with the Pacific Northwest coast (Figure 5a). These conditions are known to be favorable for updraft formation and convection (Uccellini & Johnson, 1979). There was also an approaching increase in tropospheric moisture around 850 hPa (Figure 5b). PyroCb modeling has shown midtropospheric moisture can be entrained into the convective column and contribute to instability aloft (Trentmann et al., 2006), and observational statistics of all intense pyroCbs from 2013 within North America seem to confirm this (*P*17b). Additionally, a strong low-level jet was also in place at 850 hPa which could have destabilized the planetary boundary layer (PBL) and increased the surface wind speeds near the fire (see wind barbs in Figure 5b). Ground observation sites operated by the government of the Northwest Territories recorded surface temperatures ≥32 °C, relative humidities ~20% and sustained wind speeds between 15 and 20 km/hr (see Figure S2). These are the classic hot, dry, and windy conditions associated with intense wildland fires. The traditional fire-weather indicators, the Haines Indices (Haines, 1988), were high-risk at the time of the GSL pyroCb with values of 6, 6, and 3, for the low-, mid-, and high-elevation variants, respectively. A stationary surface boundary was generating convection to the north/northwest around this time (Figure 5c), but did not appear to reach far enough south to directly impact the pyroCb location as evidenced by the lack of independent (non-pyro-) cloud formation in the immediate vicinity of the fire (see Figure 1). Therefore, with favorable conditions, but without the dynamical trigger in place to initiate the convection, we conclude that the fire itself was the trigger, and provided the necessary energy to initiate convection.

This conclusion is supported by the behavior of GOES-West normalized hourly fire radiative power (FRP) as defined by Peterson et al. (2015) and estimates of subpixel fire temperature (Giglio & Kendall, 2001) just before the GSL pyroCb began. A 36-hr time series of these values is shown in Figure 6, centered around the time of pyroconvection (green line). Normalizing the FRP in this manner accounts for potential variation in scan frequency, scattered cloud cover, and occasional invalid retrievals. Within this timeframe, the estimated fire temperature (black dots) oscillates between 500 and 700 K, but the pyroCb only forms after the strong increase in FRP (red line) just before to 18:00 UTC (12:00 local time). The FRP increased from <500 to >6,000 MW in less than 2.5 hr prior to the pyroCb, and fire temperatures increased by ~150 K over the same time. This preceding rapid increase in FRP is consistent with the conceptual model put forth in *P*17b. On this day the fire spread quickly, burning at an average rate of 2,725 ha/hr based on daily MODIS fire perimeter data, which is an order of magnitude larger than all other days on which the fire burned. The surface heat fluxes generated by such a rapid increase in FRP would certainly trigger the initial upward motion of surface and PBL parcels in an unstable atmosphere. Note the gap in FRP in Figure 6 corresponds with invalid FRP retrievals from the WF_ABBA algorithm (Prins et al., 1998), which are likely due to diminished fire activity during nighttime conditions (gray shading). At these latitudes, the GOES-West pixels are very large, so the fire would have to be extremely hot

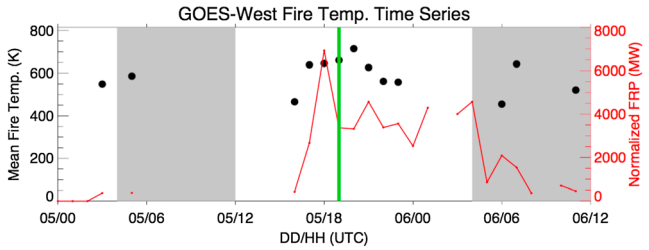

Figure 6. The 36-hr time series of normalized hourly GOES-15 FRP (red) and the mean estimated fire kinetic temperature (black) centered on the time of pyrocumulonimbus (green line). Note the large fire temperatures and peak in FRP just before initiation. Gray shading is local nighttime. Gaps in FRP are due to invalid retrievals by the WF_ABBA algorithm likely due to weak fire output in the local evening/morning. FRP = fire radiative power.

to stand out against the background, and it is likely that it was not intense enough to do that during this early morning period.

Figure 7 shows an interpolated sounding using the 5 August 12:00 UTC and 6 August 00:00 UTC soundings from the nearby Ft. Smith observation station. To construct this sounding, a temporal linear interpolation was used at each pressure to estimate the T and dewpoint temperature (T_d) at 18:00 UTC. Beneath the remaining PBL inversion, we have estimated an atmospheric temperature adjustment at this time by connecting the top of the inversion with the mean surface temperature (T_s = 34 °C) measured at nearby ground stations (red dashed line below 1 km). This adjustment gives the sounding a general appearance of the *inverted-V* type, which was also shown in *P*17b to be a typical precursor to intense pyroCb development. The convectively available potential energy (CAPE) of the sounding without the T_s adjustment is approximately 250 J/kg with an LCL of 1.8 km (not shown). This value increases to 1,985 J/kg (blue shading in Figure 7) with an LCL of 2.5 km when using the T_s adjustment. One noteworthy feature of this sounding is the moist layer of air around 450 hPa associated with the advancing trough. The dew point depression at this pressure (~4.5 °C) is the lowest in the free troposphere. Entrainment of dry air into growing convection at this pressure would typically reduce buoyancy by cooling the air through evaporation (Simpson, 1980), but it is possible that the higher relative humidity associated with this layer would limit the drying effects of entrainment, and therefore be less inhibitive to vertical cloud development. Both the conceptual model in *P*17b and case studies in Lareau and Clements (2016) show the presence of an elevated moist layer.

For pyroCb cases, it could be argued that the convective condensation level (CCL), rather than the LCL, is more appropriate to use as an estimate for cloud formation because the CCL represents the level at which a surface parcel would saturate from lifting due to heating, rather than forced dynamical uplift. However, in the case of the adjusted sounding, the CCL is found to be at an altitude ~2.6 km, which is close to the LCL. This occurs because the adjusted PBL temperatures closely follow a dry adiabatic profile. At the time the pyroCb began, T_s had almost reached the convective temperature (T_c ≃36 °C) needed to trigger free convection above the condensation level. All these arguments have been made without considering an increase to the PBL air temperature from fire-produced surface heat fluxes, which should be quite large as indicated by FRP. Thus, even though dynamical triggers were likely on the cusp of interacting with the GSL fire, and T_s was approaching T_c in nearby nonfire areas, we conclude that the fire triggered the convection.

Additional features shown in Figure 7 are the cloud boundaries seen by CALIOP and CloudSat. The overshooting top peaks at ~14 km and the cloud base (according to radar reflectivity) is near 4 km. The large difference between the LCL and the cloud base is most likely attributed to the large difference between the adjusted sounding and the actual T and T_d from surface heat flux contributions previously mentioned. Indeed, Lareau and Clements (2016) used ground-based mobile doppler lidar to show cloud bases over fires are typically much higher than LCLs determined from nearby soundings. The GSL pyroCb retrieved kinetic fire temperature was >300 °C, which leaves little doubt that the lower-most PBL lapse rate should be super-adiabatic (the (CAPE) under this condition would be on the order of 15,000 J/kg). The EL of the adjusted sounding at 12.4 km is representative of the tropopause. The gray shading in Figure 7 represents the inhibiting energy (CIN) needed to overshoot into the lower stratosphere to 14 km (CALIOP cloud top). The gray area is encompassed by this cloud top, and both the parcel temperature and sounding temperature, which have a vertex at the EL. This CIN value is 1,160 J/kg, and—using parcel theory—would necessitate an updraft velocity on the order of 50 m/s at the EL for convection to reach the observed overshoot altitude. Unfortunately, the GSL pyroCb did not occur within range of a operational doppler radar, so no confirmation can be made, but this updraft velocity is consistent with intense overshoots from regular convection that have been modeled to inject water vapor into the lower-most stratosphere (P. Wang, 2003).

An interesting feature of the GSL pyroCb is the apparent lack of precipitation during its most intense stage. The Buffalo Junction ground station (denoted by the star in Figure 1) was operating nominally at the time when the pyroCb advected over its location, and recorded no precipitation even as the wind speed peaked above 18 km/hr and surface temperature dipped by approximately 4 °C, in response to downdrafts or temporary cloud cover (see Figure S2). Despite attempts to estimate precipitation amounts with CloudSat reflectivity, the

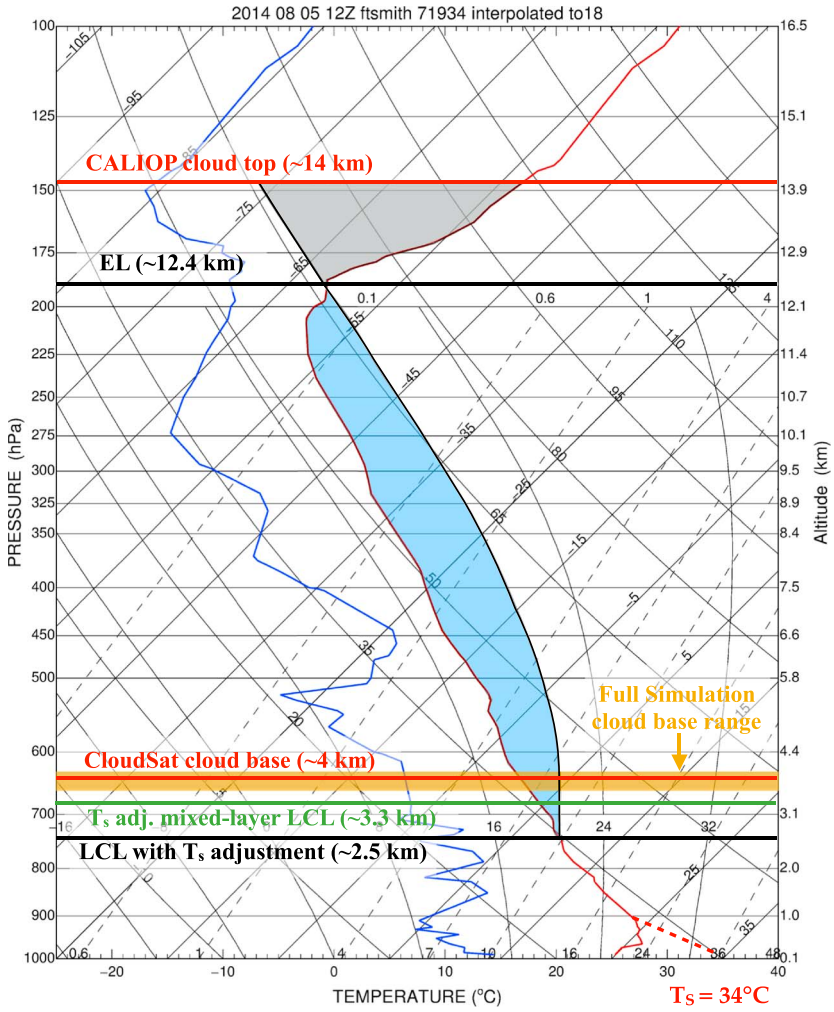

Figure 7. 18:00 UTC Ft. Smith sounding from 5 August constructed by interpolating the 12:00 and 00:00 UTC soundings. Red horizontal lines show the CloudSat and CALIOP observed cloud boundaries. The atmospheric temperature between ~900 and 1,000 hPa is shown adjusted by using the average ground station T_s (red dashed line). Using this T_s produces a CAPE = 1,985 J/kg and CIN = 1,160 J/kg (blue and gray shading, respectively). Thick black horizontal lines show the LCL and EL also computed with this T_s. Green line is the mixed-layer LCL (lowest 50 hPa) computed with the T_s adjustment. CIN is limited to pressures between the EL and the observed overshoot altitude in the lower stratosphere. The dark yellow bar between 3.7 and 4.2 km shows the range of convective cloud base heights from the Full Simulation discussed in section 4. CALIOP = Cloud-Aerosol Lidar with Orthogonal Polarization; EL = equilibrium level; LCL = lifting condensation level.

estimates are not scientifically useful over land surfaces due to a lack of reliable path-integrated attenuation (Matthew Lebsock, CloudSat product developer, personal communication). However, the CPR did measure significant reflectivity from the surface through the deepest part of the pyroCb, and Figure 4c shows a vertical gap between the surface return and the cloud base. These features provide additional confidence that there was little-to-no precipitation during the mature stage of this event. If there was any precipitation, it likely evaporated in the dryer low levels prior to reaching the surface. Note that the narrow column of radar echoes observed below the cloud base in Figure 4c is likely dense smoke/lofted debris as discussed previously.

2.2. PyroCb and Cb Comparisons

Previous studies of pyroconvection have rarely had the ability to leverage observations of the interior during the active convective stage. Some exceptions to this generality include the following: aircraft have flown through developing pyrocumulus to take radiative flux measurements (Gatebe et al., 2012), ground-based operational radar has been used to determine pyroconvective cloud tops from the uppermost echoes (Dowdy et al., 2017), and doppler lidar has been deployed to remote locations to estimate entrainment rates and

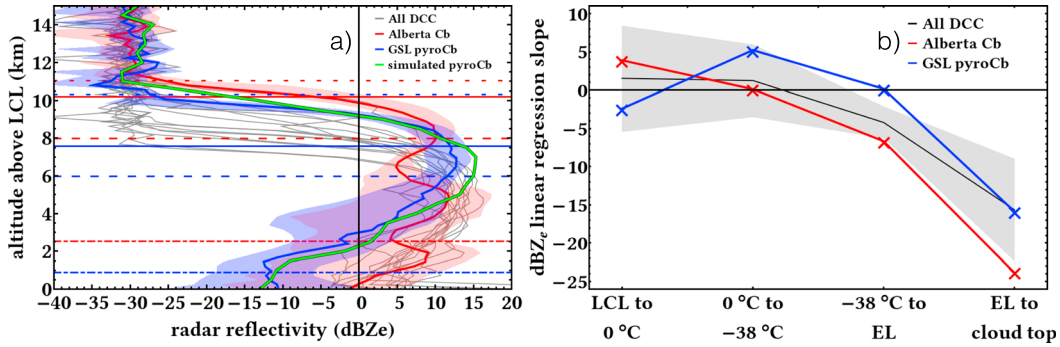

Figure 8. CloudSat horizontal-mean reflectivity profiles plotted as a function of height above the LCL through deep convection during the period 1 June to 31 August 2014 near the GSL pyroCb. Shown in (a) are the GSL pyroCb (blue), Alberta Cb (red), and the additional 15 meteorological DCC profiles identified. Blue and red shading represent the standard deviation about the mean for GSL pyroCb and Alberta Cb. Horizontal lines in (a) show freezing level (dot-dashed), homogeneous freezing level (dashed), EL (solid), and CloudSat cloud top (dotted) for both the pyroCb and Cb. Green line is the radar reflectivity from Advanced Research Weather Research and Forecasting Full Simulation pyroCb model run. (b) Black line shows the linear regression slope of mean reflectivity profiles between these thermodynamic levels and gray shading shows the standard deviation for all cases. Individual regressions of the GSL pyroCb and Alberta Cb cases are shown in blue and red, respectively. LCL = lifting condensation level; GSL = Great Slave Lake; pyroCb = pyrocumulonimbus; EL = equilibrium level.

density currents within pyroconvection (Lareau & Clements, 2016). To our knowledge, however, only one other pyroCb case has had a direct penetration of the active convective column by CloudSat and CALIOP within the ~12-year data record: the 2006 Wollemi case in Australia presented by Fromm et al. (2012). However, that CloudSat intersection occurred over 40 km to the east of the fire as the pyroCb was being advected away by strong winds, and it is possible that the CPR did not capture the full vertical depth of the cloud (see Figures 3 and 6 in that study). Thus, the current GSL pyroCb case is strategic because of contemporaneous active profiling through the updraft core of a pyroCb and nearby Cb. In this section, CPR reflectivity is used to qualitatively estimate the internal hydrometeor structure of the GSL pyroCb by partitioning the profile according to the thermodynamic levels outlined in section 2.1, and comparing it to the Alberta Cb and several other Cbs that were observed over the course of 2 months in the same region.

The mean CloudSat radar reflectivity profiles for the deep convection core (DCC) portion of the GSL pyroCb and concurrent Alberta Cb are shown in Figure 8a (blue and red lines, respectively). The shading about each of these two profiles is a horizontal standard deviation of CloudSat reflectivity within these portions of each storm. This methodology used herein to determine the DCC is similar to the algorithm used in CloudSat Level 2 Product 2B-CLDCLASS with the following variations: the assignment of vertical thermodynamic cloud boundaries, the application of MODIS thermal infrared BT selection criteria, and the additional reflectivity thresholds. We note that the 2B-CLDCLASS product is not designed to isolate DCC only, but all *deep convection*. Thus, these additional criteria are imposed to select the most intense profiles from an active updraft column, where droplet and precipitation growth are expected to occur. Here a DCC is defined using the following two sequences: first, use the colocated CloudSat ECMWF-Aux product to (a) determine the LCL altitude to use as the cloud base and (b) determine the uppermost EL, and then use the 2B-CLDCLASS to (c) find profiles with a single continuous cloud layer between the cloud base and EL, and second, use 2B-GEOPROF to (d) confirm radar reflectivity values $\geq$6 dBZ$_e$ at 8 km a.m.s.l. or $\geq$4 dBZ$_e$ at 9 km a.m.s.l., and then use Aqua MODIS to (e) confirm $BT_{11} \leq -40$ °C and (f) $BTD_{12-11} > -0.5$ °C. After the deep convection CPR profiles are identified, the reflectivities are horizontally averaged to reduce noise.

Also shown in Figure 8a are 15 additional DCC profiles from June–August identified using the above algorithm for the same region in Canada (light gray lines). More information about these cases is tabulated in Table S1. The GSL pyroCb, Alberta Cb, and all DCC profiles are plotted as a function of altitude above the cloud base (local LCL) to normalize the differences since convective cloud growth begins at the cloud base. (Note that all DCC, including the GSL pyroCb and Alberta Cb, are examined using the same cloud vertical boundary definitions: LCL for cloud base and 94 GHz threshold for cloud top. The previous discussions regarding the difference between the GSL pyroCb 94 GHz cloud base and its LCL and the differences in cloud top estimates from radar and lidar were used to illustrate the unusual nature of pyroCb only. In the following discussion, every case

is examined using constant definitions). The horizontal lines in Figure 8a represent the relevant thermodynamic levels for the pyroCb (blue) and Cb (red), and show the FL (0°; dot-dashed), HFL (−38°; dashed), the EL (solid), and the CloudSat cloud top (dotted). Here the CloudSat cloud top is defined as the lowest level above which the median reflectivity drops below the noise threshold (−28 dBZ_e) for a distance of 1 km. Defining the cloud top this way prevents spurious reflectivity values that may exist above a DCC from being identified as the cloud top. Situations with multiple cloud layers are flagged as non-DCC and ignored (i.e., the reflectivity increases above the noise threshold for a continuous altitude range at heights >1 km above a cloud top).

The pyroCb has a reflectivity of −10 dBZ_e at cloud base compared with values ranging from approximately −5 to 5 dBZ_e for the Alberta Cb and other meteorological DCC observations. The peak reflectivity for all DCC (including the GSL pyroCb) is ∼10 dBZ_e, and generally occurs between 5 and 8 km above the cloud base. The Alberta Cb shows a profile consistent with midlevel precipitation with two bright bands just beneath both the FL and HFL, whereas the GSL pyroCb profile has a more monotonic increase between the FL and HFL. Included for reference in Figure 8a is a simulated CloudSat radar reflectivity profile from the modeled GSL pyroCb discussed in section 4 (green profile). To better quantify the differences in these profiles, we computed a linear regression slope of reflectivity between the aforementioned thermodynamic levels. Figure 8b shows the values of these regression slopes for the GSL pyroCb (blue), Alberta Cb (red), and all DCC cases (black; this includes the Alberta Cb). The gray shading is the standard deviation about the mean of all meteorological DCC. The pyroCb stands out with a few interesting features: (1) reflectivity between the LCL and FL decreases by −2 dBZ_e, whereas the meteorological DCC have positive slopes, (2) there is a large positive slope (+5 dBZ_e) between the FL and HFL, with DCC having a neutral or only slightly positive slope, and (3) the pyroCb has a neutral slope between the HFL and EL, whereas all meteorological DCC are strongly negative. The pyroCb cloud base from CPR observations was shown in Figure 7 to be >1 km above the LCL, so it is no surprise that the regression slope between the LCL and FL is not positive. However, airborne debris below the cloud may be contributing to larger reflectivities at the LCL than at the FL, which would account for the negative slope (see Figure 4c).

Ignoring contributions from millimeter- or centimeter-sized biomass-burning debris, radar reflectivity at 94 GHz through a cloud is tied foremost to cloud particle size (proportional to the sixth power of particle diameter), and secondarily to the particle number concentration. As such, the profile regression slopes are primarily representative of the change in particle size with height. A positive slope indicates a growing hydrometeor size distribution between the thermodynamic levels, a negative slope indicates a diminishing size distribution, and the magnitude of these slopes indicates how rapidly or slowly these changes are occurring in the vertical. By this interpretation, the GSL pyroCb exhibited no nucleation or cloud particle growth between the LCL and FL, but was followed by intense growth in the layer between the FL and HFL. The large positive slope in reflectivity (5 dBZ_e) between these latter two levels suggests rapid growth in particle size in the mixed-phase region. This behavior is likely due to the strong updrafts produced by the release of latent heat from freezing either from an abundance of CCN, as predicted by the invigoration effect (Rosenfeld et al., 2008), or from enhanced buoyancy driven by large surface heat flux. We note that one major assumption of this interpretation is that the radar reflectivity represents condensed cloud matter only. As was seen in Figure 4, and discussed in LaRoche and Lang (2017), radar reflectivity through active pyroCb can have signatures from debris (noncloud) material, which could limit our ability to estimate size distribution growth with height from reflectivity profiles. However, as we noted in section 2 and will note again in section 4, the large debris capable of affecting reflectivity returns is typically too large to participate in cloud droplet nucleation, and additional information from CALIOP β'_{532} and MODIS BT_3 indicate a large abundance of small ice particles exists at cloud top. All this information combined gives confidence that the reflectivity profile slopes can be interpreted to represent distribution growth with height.

The slopes between the EL and cloud top are strongly negative for all cases, including the GSL pyroCb. This is because of the rapidly diminishing condensate above the EL. In the GSL pyroCb case, the regression slope between these levels is like the meteorological DCC slopes, even though the ice particles in these levels were shown to be smaller than the Cb, and should therefore have weaker reflectivity. Considering the difference in CALIOP and CloudSat cloud tops, however, the magnitude of this regression slope may be biased low because the actual cloud top (as seen by CALIOP) was located about 1 km above the CPR-observed cloud top. If the regression was computed between the EL and the CALIOP-defined cloud top, the slope would be approximately −10 dBZ_e in this layer. The CloudSat reflectivity profiles suggest that the GSL pyroCb contained many very small ice particles near the cloud top. The passive imagery with radiometrically warm BT_3 (caused by

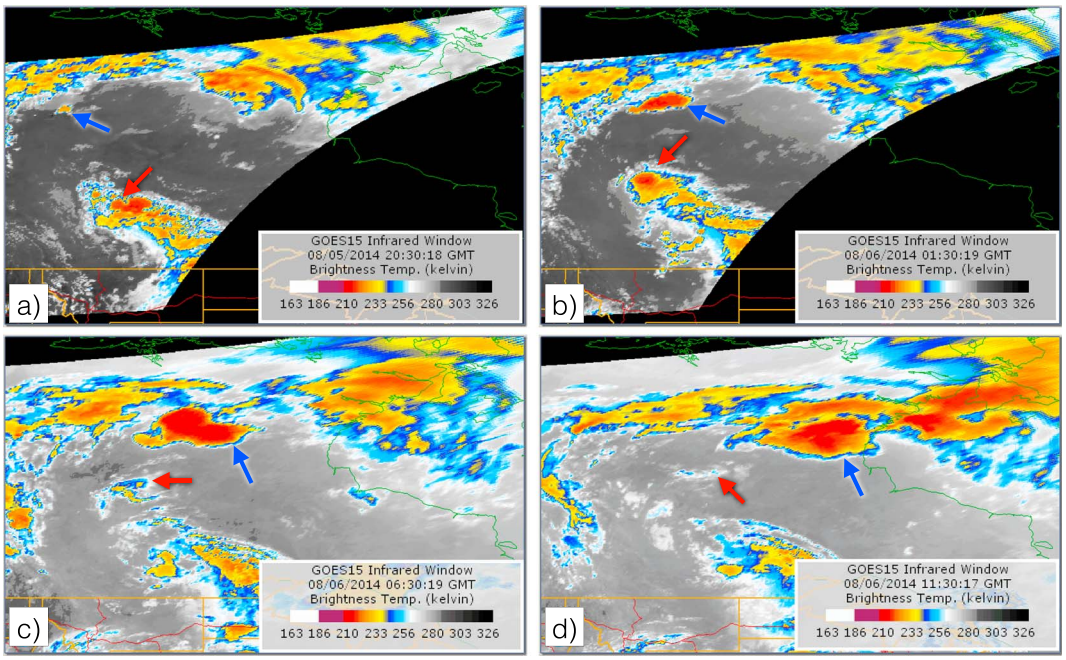

Figure 9. The 5-hourly GOES-15 IR brightness temperature imagery starting at 20:30 UTC on 5 August comparing the anvil life cycle of the Great Slave Lake pyrocumulonimbus (blue arrows) and Alberta cumulonimbus (red arrows). See Movie S2 for full animation.

enhanced solar reflectance; Lindsey et al., 2010) supports the notion of small ice particles being present near cloud top as well.

One result of this shift toward smaller, more numerous ice particles is an increase in anvil lifetime. Figure 9 contains four snapshots of GOES-15 IR BT starting at 20:30 UTC on 5 August (a) and progressing every 5 hr until 11:30 UTC on 6 August. Similar to the results of *L*08, the GSL pyroCb anvil (blue arrow) remains detectable with cold BT for much longer than the Alberta Cb (red arrow) by several hours. The pyroCb anvil actually has brightness temperature values well below the −40 °C threshold (Fromm et al., 2010) for at least 24 hr, at which point it becomes indistinguishable from nearby meteorological cirrus. On the other hand, the Cb anvil dissipates almost completely within the 12 hr depicted in Figure 9. A 25-hr animation of this GOES-15 imagery beginning at 19:30 UTC on 5 August is provided in the supporting information (Movie S1). It is possible that upper-level descending air from a synoptic ridge contributed to the Cb anvil dissipating quicker than the pyroCb anvil, but the magnitude of this effect is unknown. However, in the next section we show that the ice within the pyroCb anvil remained detectable for greater than 5 days postdetrainment, which is several days longer than midlatitude meteorological Cb anvils (*L*08).

3. Detrained Stratospheric Plume Properties

The detrained plume from the GSL pyroCb anvil was observed multiple times by A-Train instruments over the subsequent 2 weeks following 5 August. In particular, CALIOP and Microwave Limb Sounder (MLS) were able to capture the particle and gaseous constituents, respectively. One of the objectives of this study is to quantify what effect this plume had on the downstream water vapor mixing ratio (WVMR) concentrations. To that end, we have computed a climatology of WVMR using all available Level 2, Version 4 MLS H_2O data from the years 2005 to 2014 (Livesey et al., 2018) for the months of June–August. MLS H_2O data are retrieved on pressure surfaces and are considered scientifically valid for pressures $\lesssim$316 hPa. Since the focus is on the UTLS, we use the MLS Temperature product to convert these pressures to potential temperatures (θ), and then average the vertically resolved H_2O profiles on isentropic levels. All data from this time period are then averaged on a 10° × 5° (longitude × latitude) grid. Individual plume anomalies are then computed by subtracting the three-dimensional climatology from observed values in each MLS profile. We use the MLS GPH product to approximate the altitude above mean sea level of the vapor anomalies for colocation with the CALIOP profiles.

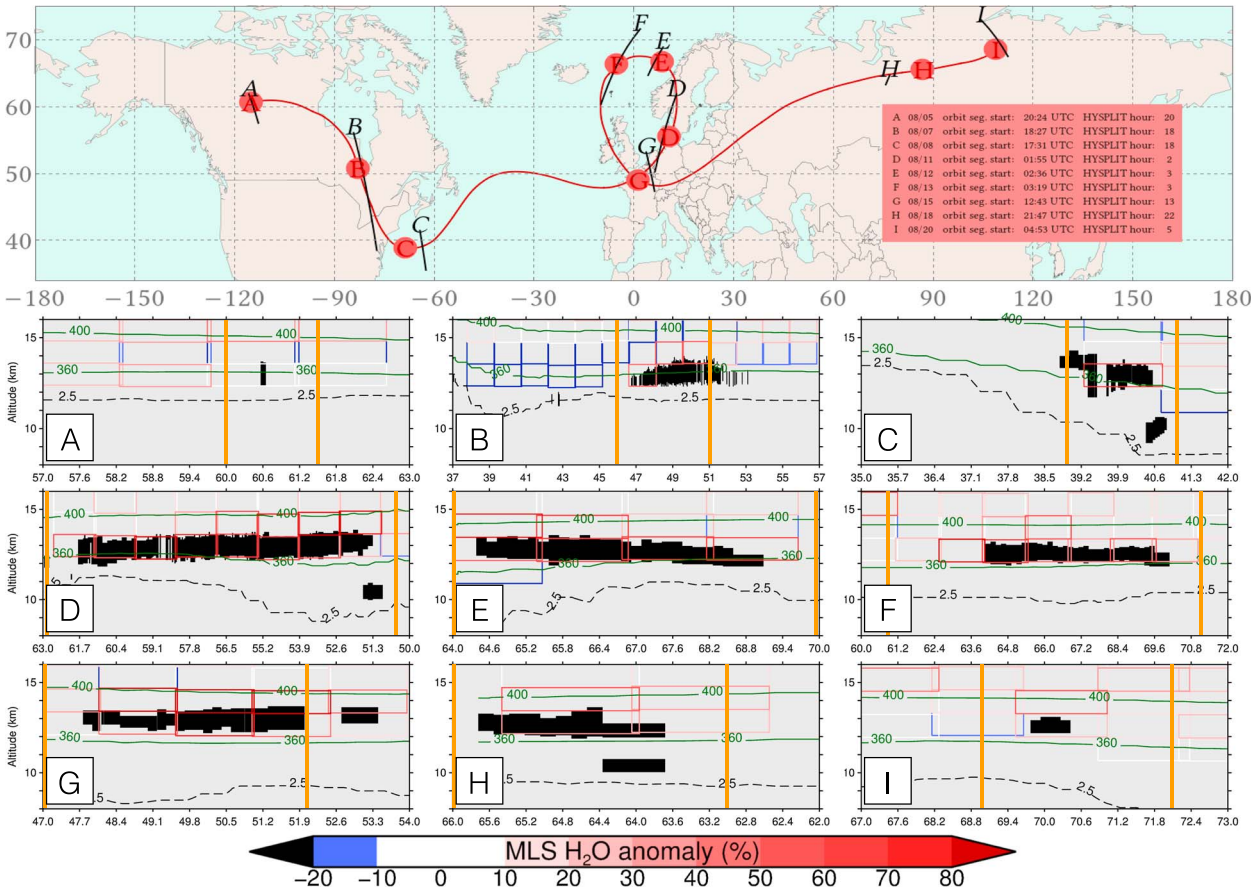

Figure 10. (Top) Map of Hybrid Single-Particle Lagrangian Integrated Trajectory model trajectory showing intersections with relevant A-Train orbits. Segments are labeled A–I, and the date, segment time stamp and corresponding Hybrid Single-Particle Lagrangian Integrated Trajectory model hour are given in the inset table. (A–I) CALIOP Vertical Feature Mask curtains showing the *stratospheric features* in black with MLS water vapor anomalies overlaid as colored rectangles (% relative to local climatology). Black dashed line is 2.5 PVU dynamical tropopause and green contours are potential temperature (K) from ERA-I reanalysis. Abscissae of A–I are in degrees of latitude, and orange vertical lines bound the curtain profiles used in Figures 11 and 12. Corresponding β'_{532} curtains are shown in Figure S3.

This step ensures that the analyzed vapor concentrations are spatiotemporally concomitant with any stratospheric aerosol/ice layer identified using CALIOP.

Figure 10 shows the path the plume followed and the individual curtain plots of CALIOP and MLS over the 2 weeks post-UTLS injection. The map in the upper panel contains a Hybrid Single-Particle Lagrangian Integrated Trajectory model (HYSPLIT) forward trajectory (Stein et al., 2015) initialized from the first A-Train observation segment (denoted with an "A") on 5 August. Additional observations are noted along the trajectory with eight orbit segment nadir-tracks denoted with letters B–I. The plume made its way eastward over the Atlantic during the week following injection, and then it made a cyclonic loop around western Europe between 10 and 15 August as the winds in the UTLS were being driven by a baroclinic storm. Over the following days it moved over northern Asia as the CALIOP backscatter signal weakened, until it became undetectable after 20 August. These detections were corroborated using the nearest HYSPLIT hour that matched the orbit segment (red circles along the trajectory). MLS WVMR was synchronized with CALIOP backscatter, and the WVMR anomaly was computed using the climatology at that location.

The nine panels below the map in Figure 10 correspond with the A–I observations locations. Each of these panels contains the CALIOP *stratospheric feature* as defined in the Level 2 Vertical Feature Mask product, which is determined in part by a the presence of β'_{532} above molecular background levels in the stratosphere. Also shown are the MLS water vapor anomaly in percent (open squares plotted to match the limb-sounding measurement volume geometry), the 2.5 PVU isosurface used to approximate the dynamical tropopause location (black dashed line), and the θ = 360, and 400 K isentropes (green lines). Note the good correspondence

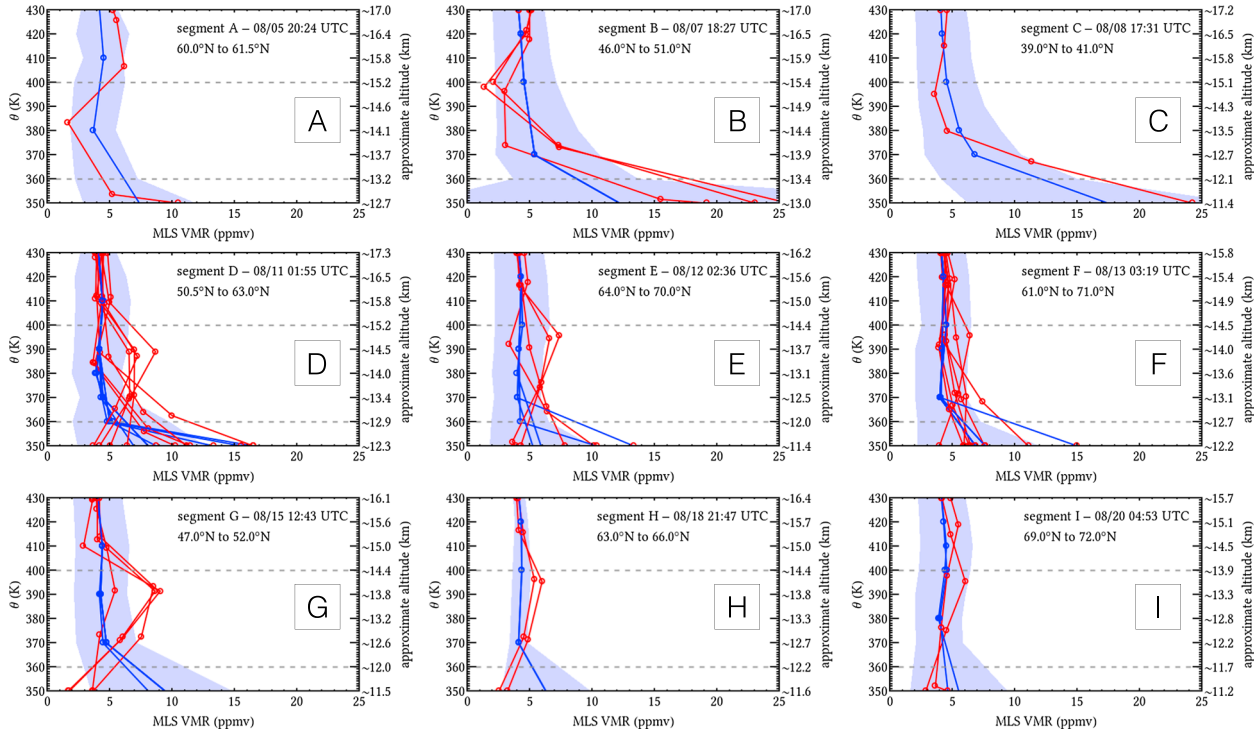

Figure 11. MLS water vapor profiles through the pyroCb plume (red lines) observations shown in Figure 10. Blue lines are the profiles of background WVMR from the 2005 to 2014 June-July-August gridded climatology that fall within the region bounded by orange lines in panels A–I in Figure 10, blue shading shows the standard deviation of these background profiles. The gray dashed lines delineate the potential temperature boundaries of the plume over the course of its observable lifetime. MLS = Microwave Limb Sounder; WVMR = water vapor mixing ratio.

between the positive WVMR anomalies and the plume locations in the stratosphere at each observation (segments B–I) after the primary injection from the active pyroCb (segment A). Many of the MLS observations contain anomalous WVMR values >80% surrounding the CALIOP plume locations (orange vertical lines on panels A–I encompass the MLS and CALIOP data presented in Figures 11 and 12). See Figure S3 for corresponding views of β'_{532}.

Individual profiles of the WVMR values corresponding with these plume intersections are shown in Figure 11, plotted here using potential temperature as the vertical coordinate. Approximate altitude from the GPH product is shown on the right-side ordinate axis. The red lines are the absolute magnitude (not the anomaly) of the WVMR observation, and the blue lines represent the climatology values that correspond with the plume-portion of the orbit segment shown in the Figure 10 map. To help orient the viewer, the individual curtains shown in Figure 10A–I span a larger latitude range than the plume width denoted on the Figure 11A–I panels. Horizontal gray dashed lines mark the 360 and 400 K isentropic boundaries to which the plume was confined during its observable lifetime. Note the increase in WVMR at θ = 390 K ranging from 1 to 5 ppmv greater than the climatology as the plume ages and undergoes the cyclonic movement in segments D–G. In the two final segments (H, I), individual WVMR anomalies are still as large as 2 ppmv above climatological values.

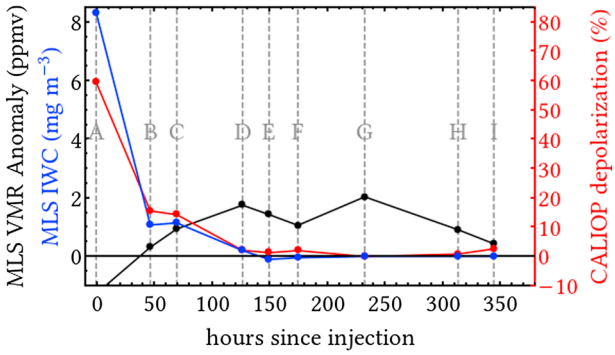

Figure 12. Mean values of MLS WVMR anomalies and IWC and median CALIOP δ_{532} over the 2-week observable lifetime of the plume. Each MLS point in this time series represents a per-profile vertical mean between 360 and 400 K for measurements encompassing the plume (dashed lines in Figure 11), and each CALIOP point is the median value for the entire *stratospheric feature* between 360 and 400 K. MLS = Microwave Limb Sounder; WVMR = water vapor mixing ratio; IWC = ice water content; CALIOP = Cloud-Aerosol Lidar with Orthogonal Polarization.

The pyroCb injected a large abundance of small ice particles combined with smoke that underwent diffusion over the subsequent days. To test the hypothesis of ice sublimation increasing downstream absolute humidity within the plume we combine these WVMR anomalies with MLS retrievals of ice water content (IWC). In Figure 12 we show a time series of the MLS WVMR anomalies (black line) along with corresponding MLS IWC

observations (blue line) and CALIOP depolarization ratio (δ_{532}, red line). For this time series, δ_{532} was computed from Level 1 CALIOP backscatter, and contains the median value of pixels only contained within the Vertical Feature Mask stratospheric features in Figure 10A–I. Vertical gray dashed lines denote the times of each orbit segment. The MLS values plotted here are averaged between 360 and 400 K for the plume locations within each orbit segment. The initial A-Train observation (A; hour 0) has an IWC value of 8.3 mg/m^3, and then over the next 50 hr reduces to 1 mg/m^3, at which point the WVMR anomaly has become positive. Over the subsequent 100 hr, IWC diminishes to 0 mg/m^3 as the WVMR anomaly increases to a plume-averaged value of ~2 ppmv (+45%), and remains large for the next three observations (segments E–G). After the plume has aged 350 hr, there are no more detections made by the A-Train that can confidently be attributed to the pyroCb source. CALIOP depolarization ratio is examined as an additional test for ice presence. On a pixel-by-pixel basis, values of δ_{532} should approach 50% when significant amounts of ice are present (Hu et al., 2009). As shown here, δ_{532} closely mimics MLS IWC behavior. At the initial injection observation (A) δ_{532} is ~60%, and quickly diminishes to ~15% when the plume is 50–70 hr old (B,C). By the next observation (D; near hour 125), δ_{532} is less than 5% and remains low for the rest of the observable lifetime. Taken together, it is apparent that the WVMR increases as ice presence decreases.

4. ARW Model Simulations

To estimate the sensitivity of the GSL pyroCb to specific variables, we employ the nonhydrostatic and compressible Advanced Research Weather Research and Forecasting (ARW) model. The model is run for four conditions. First, a control pyroCb simulation is established using the geography and weather forcing of the GSL pyroCb event (Full Simulation). The remaining three model runs are repeats of the Full Simulation with individual alterations to initial conditions. The second simulation has aerosol concentrations over the fire reduced to background values (Low Aerosol), the third has reduced moisture advection in the PBL and free troposphere (Low Moisture), and the fourth has surface sensible and latent heat fluxes reduced to background values (Low Heat Flux). The purpose of these simulations is to test the effect of surface CCN concentrations, moisture entrainment, and surface heating on pyroCb cloud properties.

4.1. Model Setup

The simulations are run for a 24-hr period starting at 12:00 UTC on 5 August and ending at 12:00 UTC on 6 August. The nearby soundings from Ft. Smith discussed in section 2.1 are used to force the model with tendencies in potential temperature and specific humidity—interpolated from these soundings—and are used to represent temperature and humidity advection. A fifth-order monotonic advection scheme is used for the advection of cloud variables (H. Wang et al., 2009), and radiation is handled with the one-dimensional Rapid Radiative Transfer Model (Fouquart & Bonnel, 1980; Mlawer et al., 1997). To capture the mesoscale structure of the pyroCb, and to resolve cloud processes, the model horizontal domain is set to 200 × 200 km^2 using a 500 m resolution and a domain depth of 20 km at 200 m resolution. A bulk double-moment microphysics parameterization is used that emulates a bin microphysics scheme for the calculation of collection and sedimentation processes. This parameterization is generally referred to as the bin-bulk scheme and was first implemented into Regional Atmospheric Modeling System at Colorado State University (Saleeby & Cotton, 2008; Walko et al., 1995).

For the Full Simulation, the surface sensible and latent heat fluxes are set to 150 and 310 W/m^2, respectively, in the nonfire regions of the domain. A hot spot representing the fire is modeled as a circle centered in the domain with diameter = 20 km, and sensible and latent heat fluxes are set to 15,000 and 1,800 W/m^2, respectively. All heat flux values for the background and hot spot are based on the previous modeling studies by Trentmann et al. (2006) and Luderer et al. (2006), which used boreal forest emissions for a *reference simulation*. Values from that simulation are used in the present study. Beringer et al. (2003) noted that sensible heat fluxes are much greater than latent heat fluxes over fire (large Bowen Ratio), and Trentmann et al. (2006) noted that there exists a positive feedback between these fluxes due to increased entrainment of low-level moisture as a fire emits more sensible heat. In the present model setup, this interaction is ignored, and all heat values are prescribed without any meteorological coupling. The heat fluxes are also temporally invariant throughout the simulation period. Therefore, the results here are not designed to mimic reality with respect to fire-atmosphere interaction, but are idealized so that sensitivity of convective properties between model runs can be more readily compared. Directly over the fire, the aerosol concentration is set to 15,000 cm^{-3} within the PBL, and decreases exponentially with height in the free troposphere. Within the PBL at nonfire locations, the concentration is set at 150 cm^{-3}, also decreasing exponentially with height above this level.

A big question regarding pyroCb development is the individual effects of surface heat fluxes, fire-produced aerosol particles, and moisture entrainment illustrated by *P*17b. Toward the goals of assessing convective intensity, properties of detrained cirrus, and impacts on UTLS moisture, it is useful to rerun the control simulation with high heat flux/low aerosol and with low heat flux/high aerosol. To estimate the effect of the former, the Low Aerosol simulation is done by repeating the Full Simulation with PBL aerosol concentrations reduced to the background level (150 cm^{-3}) over the fire. Then, to estimate the role played by surface heat fluxes, the Low Heat Flux run maintains the large aerosol concentrations of the Full Simulation, but has reduced surface latent and sensible heat fluxes to the background values (310 and 150 W/m^2, respectively) within fire spot. However, for these conditions, it is found that surface latent and sensible heat fluxes in the fire spot are too low to form a cloud, so a potential temperature perturbation is prescribed over the fire spot to trigger a cloud, following Weisman and Klemp (1982). The horizontal extent of this perturbation is identical to that of the fire spot and the vertical extent is 2.8 km, and the maximum perturbation is 1.8 K. This perturbation has been used by numerous previous studies and considered to have negligible influences on cloud development, although it triggers the formation of a cloud.

As discussed in section 2.1, the GSL pyroCb occurred during a substantial advection of moisture in the midtroposphere. North American Regional Reanalysis data also showed an immediate increase in surface relative humidity at the time of convection (20–30% → 50–60%). It is possible this advection contributed a significant amount of moisture to the atmosphere over the fire—and therefore instability—just before pyroCb formed, or that it was entrained during convection. To test whether these moisture sources had any impact on convection, the Full Simulation run is repeated again by reducing the level of moisture advection by a factor of 5 in the lower free troposphere (2.5–3.5 km) throughout the simulation period (Low Moisture run). Since the simulations are started about 6 hr prior to the formation of the pyroCb, this reduction is applied to the period before and after convection starts to limit entrainment from both the surface through the cloud base and the free atmosphere through the sides of congestus.

4.2. Results

In Figure 1, the pyroCb anvil is observed to advect to the northeast of the fire spot due to the southwesterly winds at the outflow altitude. In the Full Simulation, a convective column forms over the fire spot, and is accurately advected northeastward as the GSL pyroCb does in reality. Figure 13 shows the field of cloud ice mixing ratio (representing the outflow anvil) at the ~13 km EL of the simulated pyroCb approximately 3 hr after convection began (VIIRS image in Figure 1f). The modeled anvil cirrus cloud is ~80 km in diameter and generally agrees with the VIIRS cloud location as the cirrus has advected to the northeast. The distance between the bulk of the simulated cirrus and the fire (~100–120 km) is slightly greater than the VIIRS observation (~90–100 km) at this time, however. Figure 8 shows a vertical profile of the simulated 94 GHz radar reflectivity plotted above the cloud base (green line) corresponding to the CloudSat overpass time of 20:20 UTC (~2 hr after the simulated convection began). The shape of the Full Simulation profile reasonably matches the shape of the GSL pyroCb CloudSat profile, indicating the model represents the high cloud base and overall vertical structure reasonably well. The pyroconvection cloud base height from the Full Simulation varies between 3.7 and 4.2 km above the surface for the duration. Note that this cloud base height agrees well with the observed CloudSat CPR-derived cloud base, and not the envrionmental LCL (Figure 7). The net effect of the heat fluxes and convection on the atmospheric temperature profile are determined following Trentmann et al. (2006) and show a positive temperature anomaly of +53 K at 0.1 km above the surface, and quickly reduce to +18 K at 2.0 km, +5 K at 4 km, and 0 K at 6 km.

As mentioned previously, heat fluxes over fires can produce extremely large updrafts from enhanced buoyancy, but increased CCN concentrations are also known to enhance updrafts from latent heat release (Reutter et al., 2014). The results of Luderer et al. (2006) showed heat fluxes dominate the updraft velocities over aerosol influences, and that result is confirmed here. Figure 14a shows the vertical distributions of the time- and domain-averaged updraft mass flux—a standard representation of the cloud dynamic intensity—for all four model runs. The black line is the Full Simulation, which has a peak value of 3.2 $kg{\cdot}m^{-2}{\cdot}s^{-1}$ at the top of the PBL. The bump in the updrafts between 8 and 11 km is due to a buoyancy push from the latent heat of freezing. The Low Aerosol run (blue line) closely follows the Full Simulation profile throughout the depth of the troposphere with minimal deviation. The impact of limiting the entrainment of advected moisture (green line) is slightly stronger than limiting aerosol concentrations. Although this profile is similar to the Full Simulation mass fluxes, the model shows a greater reduction in updrafts, especially between 7 and 9 km where mass fluxes are 10–15% less than the Low Aerosol run. This implies that any invigoration from an aerosol

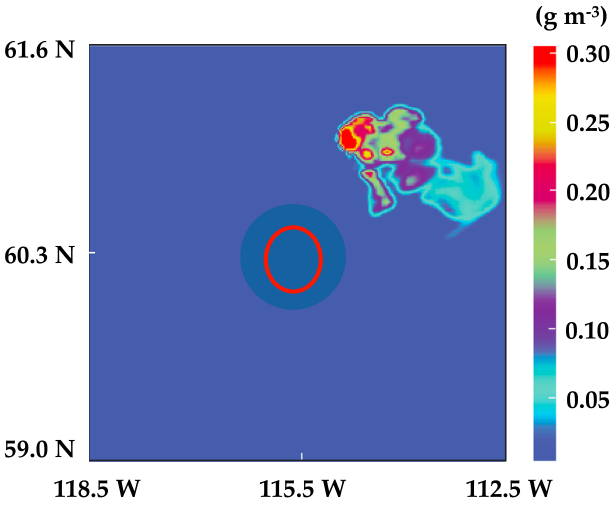

Figure 13. Advanced Research Weather Research and Forecasting Full Simulation ice particle mixing ratio within the cirrus outflow at the equilibrium level (~13 km) during the mature stage of pyroconvection (approximately 3 hr after convection began). Red circle denotes fire hot spot location used to initialize the simulation. Compare with Visible Imaging Infrared Radiometer Suite image in Figure 1f.

increase is likely dependent on the availability of moisture. However, the largest impact on updraft mass flux is from a reduction in surface heat fluxes (red line), which is ~4 times smaller than the other runs. Limiting sensible and latent heating from the fire down to background values produces a peak updraft mass flux of 1.1 kg·m^{-2}·s^{-1} and a upper tropospheric peak of ~0.3 kg·m^{-2}·s^{-1}. Among the variables tested here, this result confirms fire-induced surface heat fluxes play the most important role in pyroCb intensity. The updraft velocity for the Full Simulation has a maximum of 52.5 m/s, closely matching the buoyant energy estimate in section 2.1, and a mean of 23.3 m/s.

The different model runs produce comparable differences in cloud ice mass densities (Figure 14b). Similar to the updraft mass fluxes, the fire-induced surface heat fluxes play the most important role in the amount of cloud ice particularly just below the tropopause. The ice mass density peaks ~12.8 g/m^3 at the EL for the Full Simulation with minimal reductions in the Low Aerosol and Low Moisture runs (~11.5 and ~10.8 g/m^3, respectively). Of the various ways that surface heat fluxes, moisture entrainment, and aerosol concentrations may influence ice cloud properties, the common mechanism is updraft buoyancy. Hence, these ice mass densities are not surprising given the updrafts shown in Figure 14a. The additional mechanism to consider is an increased number density of ice particles caused by an increased droplet number density from CCN nucleation. This mechanism is one of the bases for invigoration theory, which predicts that an initial suppression of precipitation in lower levels leads to more condensate reaching the HFL. The theory involves increases in latent heat release, updrafts and deposition, and decreases in the size of ice particles. These changes favor the enhancement of ice mass density at cirrus levels, since deposition is a main source of ice mass and the smaller size of the particles causes smaller terminal velocity and thus less efficient removal of the particles via sedimentation. Figure 14b shows that this mechanism does not seem to have much influence on the ice mass density because the Low Aerosol result does not deviate significantly from the Full Simulation result. The interaction between surface aerosol concentrations and nucleation of condensate is explicitly accounted for in these simulations, so the minimal impact that surface CCN concentration has on pyroCb ice density is likely due to the updraft velocity being dominated by surface heat fluxes.

Vertical distributions of the averaged WVMR from all four simulations are shown in Figure 15, plotted above the model tropopause (13 km). These values (solid lines) are spatiotemporally averaged over the simulation in all areas with nonzero liquid and ice water path. Again, there are differences between WVMR values from the Full Simulation and the other three runs, but the Low Heat Flux run has the most significant deviation. For example, at 14 km the Full Simulation has an average WVMR = 15 ppmv, the Low Aerosol run has 14 ppmv, the Low Moisture run has 11 ppmv and the Low Heat Flux run is near 7 ppmv. These values, however, do not account for sublimation from the aging ice cloud detrained at these altitudes. Combining these WVMR values

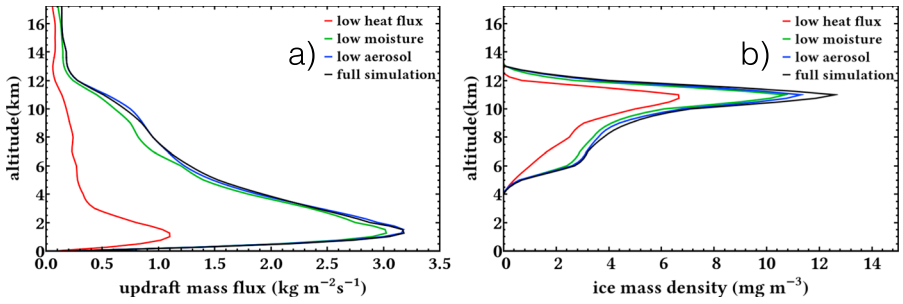

Figure 14. Profiles from four pyrocumulonimbus model simulations showing the averaged vertical distributions of the (a) spatiotemporally averaged updraft mass fluxes and (b) ice mass densities. See text for descriptions of the four simulations.

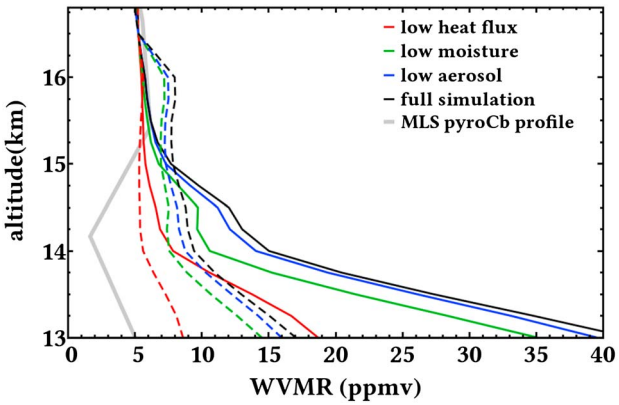

Figure 15. Profiles of WVMR spatiotemporally averaged for each simulation for all cloud regions within the domain (solid lines), and surviving water postdetrainment (dashed lines), estimated here to be 30%. The latter includes vapor contributions from ice sublimation and existing absolute humidity. The MLS observation during the active pyrocumulonimbus—when no WVMR enhancement is yet present—is shown as a gray line as a reference to the background profile. WVMR = water vapor mixing ratio; MLS = Microwave Limb Sounder.

with the vapor contribution from ice would provide the maximum total water available, which at 14 km is approximately 27 ppmv for the Full Simulation, reducing down to 14 ppmv for Low Heat Flux (not shown).

MLS observations showed the GSL pyroCb plume WVMR peak between 8 and 9 ppmv near 14 km after about 1 week (see Figure 11D,E). Using this as a reference, we estimate that there should be approximately a 30% survival of total water from both detrained vapor and sublimated ice in order to reach these values at Days 6–7 of the plume's lifetime. This 30% survival estimate is applied to each model run and shown as dashed lines in Figure 15. The cloud ice mass density from each simulation is converted to parts per million and is combined with the molecular water vapor and multiplied by 0.3. At 14 km, the value from the Full Simulation is between 9 and 10 ppmv, the Low Aerosol is 8–9 ppmv, the Low Moisture is 7–8 ppmv, and the Low Heat Flux is ~5 ppmv. As the plume ages to its last MLS observation (Day 15; Figure 11I), the vapor concentrations have reached background levels (4–5 ppmv), which for the Full Simulation would mean >10% of the initially injected total water remains in plume. We caution that this is a simplified interpretation of how a detrained UTLS plume may evolve, and also note that the model simulations produce a peak in total water around 16 km, but no enhancements were observed at these altitudes by MLS. Since our survival calculation takes into account only the instantaneous profiles of total water postconvection, there are likely several physical processes that are being neglected such as the sedimentation of ice to lower levels, and any subsequent entrainment/mixing that may occur due to convective turbulence. While these estimates are in no way exhaustive, they provide a possible starting point for further study into how sublimation rates from detrained ice clouds could affect the vapor mixing ratio downstream.

5. Conclusions

A case study of the GSL pyroCb from 5 August 2014 in Northwest Territories of Canada was presented using satellite- and ground-based observations, and multiple ARW cloud-resolving simulations. This pyroCb was an intense storm that penetrated the tropopause, reaching up to ~14 km ($\theta \simeq 380$ K). Passive imagery from MODIS, VIIRS, and GOES-West detailed the convective life cycle of this pyroCb and allowed for comparisons with a concurrent Cb that formed to the south in Alberta. BT at thermal- and near-infrared channels indicated the cloud had a large number density of ice particles with a very small effective radius. CloudSat and CALIOP made fortuitous intersections within a few minutes of the active core of both the GSL pyroCb and the Alberta Cb and allowed for direct comparison of the internal structure of the storms based on radar reflectivity profiles. Additional deep convective core (DCC) cases from June–August in the same region were identified using the CPR and also analyzed. The pyroCb had radar reflectivity profiles that indicated a suppression of precipitation, and rapid hydrometeor growth between the FL and the HFL, whereas the Alberta Cb and the 15 other meteorological DCC had reflectivity profiles showing the presence of precipitation, and smaller changes in radar reflectivity between the FL and HFL.

An analysis of the meteorology indicated that the GSL pyroCb formed in favorable convective conditions, but FRP retrievals from GOES-West and a lack of meteorological trigger showed that the fire itself likely initiated the convection. Surface observations from the Buffalo Junction ground station, over which the pyroCb advected during the active convective stage, showed no precipitation reached the surface. GOES-West showed the GSL pyroCb anvil was detectable in thermal infrared imagery for at least 24 hr until it became indistinguishable from nearby (and lower altitude) cirrus clouds. This lifetime was approximately 50% longer than the Alberta Cb anvil, which is in agreement with anvil lifetime results published by *L*08. The detrained GSL pyroCb anvil was tracked in the lower stratosphere over 2 weeks using a combination of HYSPLIT trajectories and CALIOP observations of the aerosol/ice plume. Concurrent MLS observations of this plume indicated that ice was present initially, but sublimated within a week. MLS also observed a substantial increase in WVMR values over this time that produced plume-averaged anomalies as large as 2 ppmv (>50%) relative to a 2005–2014 climatology. In general, these WVMR anomalies appeared to be anticorrelated with IWC

observations, which implies aging pyroCb plumes that undergo ice sublimation could enhance WVMR on short timescales.

Idealized Simulations of the GSL pyroCb using ARW showed that updraft mass fluxes, cloud ice concentrations, and detrained WVMR were heavily influenced by the surface sensible and latent heat fluxes prescribed over the fire. Sensitivity tests on other initial conditions, such as lowering the surface aerosol concentrations and limiting the moisture entrainment indicated these had a smaller effect. These tests were performed using a full simulation of the GSL pyroCb as a control. Although the pyroCb was less sensitive to both aerosol and moisture entrainment, the aerosol concentration had the least influence. This approach is unique from most convective modeling studies in that the control is based on the most intense situation (pyroCb). Other convective modeling studies have found that aerosol increases substantially impact updraft intensity and microphysics (Fan et al., 2013; Khain et al., 2005), although the impact strongly dependent on environmental conditions such as stability, humidity, and wind shear (Khain et al., 2008; Lee et al., 2008), but when starting with a pyroCb, the model showed that aerosols are not nearly as important as the surface heat fluxes. This case agrees with previous idealized pyroCb modeling (Reutter et al., 2014). The ARW simulations shown here also indicated there is a substantial amount of vapor detrainment in the case of the GSL pyroCb, but by itself the absolute humidity is not enough to match MLS observations of the plume 1 week later. We estimate that a 30% survival of all water produced in the model (including both sublimation from ice clouds and absolute humidity detrained at cloud top levels) would account for the 7–9 ppmv values observed in the aging plume. However, these simulation results should be considered preliminary, and provide a basis for future work.

The observations made by the A-Train and the ARW model results indicate that lower stratospheric water vapor may be influenced by pyroCb activity, at least on short time scales. As recent studies have shown, these pyroCb events are a relatively common occurrence every season (Peterson, Fromm, et al., 2017). Given the radiative significance of this greenhouse gas in the UTLS, it is worth considering a larger research effort into understanding the net impact that these events may have.

Acknowledgments
The authors would like to thank Franco Nogarin from the Canadian Environment and Natural Resources department within the Government of the Northwest Territories for providing ground station data and Mike Smith from Yukon Wildland Fire Management for providing photography and an on-the-ground description of events of 5 August 2014. We would also like to thank Dan Lindsey for creating imagery, Mike Flannigan for MODIS fire perimeter data, and Brian Potter and Rick McRae for beneficial discussion and valuable feedback. We also thank Neil Lareau and two anonymous additional reviewers for enhancing the quality of this manuscript with valuable reviews. This work was supported in part through National Aeronautics and Space Administration (NASA) grants NNH15ZDA001N and NNX16AN61G, Office of Naval Research grant N00014-16-1-2040, the NOAA JPSS Program Office and the Jet Propulsion Laboratory, California Institute of Technology under a contract with NASA. Data used in this study can be obtained as follows: CloudSat; Cooperative Institute for Research in the Atmosphere (http://www.cloudsat.cira.colostate.edu/data-products), VIIRS; NOAA Comprehensive Large Array-Data Stewardship System (http://www.bou.class.noaa.gov/), CALIOP; NASA Langley Research Center (http://eosweb.larc.nasa.gov/HBDOCS/langley_web_tool.html), MODIS; Level 1 and Atmosphere Archive & Distribution System (http://ladsweb.modaps.eosdis.nasa.gov/archive/allData/61/), MLS; Goddard Earth Sciences Data and Information Services Center (http://acdisc.gesdisc.eosdis.nasa.gov/data/Aura_MLS_Level2/), GOES; NOAA Weather and Climate Toolkit (http://www.ncdc.noaa.gov/wct/).

References

Austin, R., Heymsfield, A., & Stephens, G. (2009). Retrieval of ice cloud microphysical parameters using the CloudSat millimeter-wave radar and temperature. *Journal of Geophysical Research*, *114*, D00A23. https://doi.org/10.1029/2008JD010049

Banta, R., Olivier, L., Holloway, E., Kropfli, R., Bartram, B., Cupp, R., & Post, M. (1992). Smoke-column observations from two forest fires using Doppler lidar and Doppler radar. *Journal of Applied Meteorology*, *31*(11), 1328–1349.

Bedka, K. (2011). Overshooting cloud top detections using MSG SEVIRI Infrared brightness temperatures and their relationship to severe weather over Europe. *Atmospheric Research*, *99*(2), 175–189.

Beringer, J., Hutley, L., Tapper, N., Coutts, A., Kerley, A., & O'grady, A. (2003). Fire impacts on surface heat, moisture and carbon fluxes from a tropical savanna in northern Australia. *International Journal of Wildland Fire*, *12*(4), 333–340.

Caffrey, P., Fromm, M., & Kablick III, G. (2018). WRF-Chem simulation of an East Asian dust-infused baroclinic storm (DIBS). *Journal of Geophysical Research: Atmospheres*, *123*, 6880–6895. https://doi.org/10.1029/2017JD027848

Damoah, R., Spichtinger, N., Servranckx, R., Fromm, M., Eloranta, E., Razenkov, I., et al. (2006). A case study of pyro-convection using transport model and remote sensing data. *Atmospheric Chemistry and Physics*, *6*(1), 173–185. https://doi.org/10.5194/acp-6-173-2006

Delanoë, J., & Hogan, R. (2010). Combined CloudSat-CALIPSO-MODIS retrievals of the properties of ice clouds. *Journal of Geophysical Research*, *115*, D00H29. https://doi.org/10.1029/2009JD012346

Dowdy, A., Fromm, M., & McCarthy, N. (2017). Pyrocumulonimbus lightning and fire ignition on Black Saturday in southeast Australia. *Journal of Geophysical Research: Atmospheres*, *122*, 7342–7354. https://doi.org/10.1002/2017JD026577

Fan, J., Leung, L., Rosenfeld, D., Chen, Q., Li, Z., Zhang, J., & Yan, H. (2013). Microphysical effects determine macrophysical response for aerosol impacts on deep convective clouds. *Proceedings of the National Academy of Sciences of the USA*, *110*(48), E4581–E4590.

Fouquart, Y., & Bonnel, B. (1980). Computations of solar heating of the Earth's atmosphere: A new parameterization. *Contributions to Atmospheric Physics*, *53*, 35–62.

Fromm, M., Kablick III, G., & Caffrey, P. (2016). Dust-infused baroclinic cyclone storm clouds: The evidence, meteorology, and some implications. *Geophysical Research Letters*, *43*, 12643–12650. https://doi.org/10.1002/2016GL071801

Fromm, M., Lindsey, D. T., Servranckx, R., Yue, G., Trickl, T., Sica, R., et al. (2010). The untold story of pyrocumulonimbus. *Bulletin of the American Meteorological Society*, *91*(9), 1193. https://doi.org/10.1175/2010BAMS3004.1

Fromm, M., McRae, R., Sharples, J., & Kablick III, G. (2012). Pyrocumulonimbus pair in Wollemi and Blue Mountains National Parks, 22 November 2006. *Australian Meteorological and Oceanographic Journal*, *62*(3), 117–126.

Fromm, M., & Servranckx, R. (2003). Transport of forest fire smoke above the tropopause by supercell convection. *Geophysical Research Letters*, *30*(10), 1542. https://doi.org/10.1029/2002GL016820

Fueglistaler, S., Dessler, A., Dunkerton, T., Folins, I., Fu, Q., & Mote, P. (2009). Tropical tropopause layer. *Reviews of Geophysics*, *47*, RG1004. https://doi.org/10.1029/2008RG000267

Gatebe, C., Varnai, T., Poudyal, R., Ichoku, C., & King, M. (2012). Taking the pulse of pyrocumulus clouds. *Atmospheric Environment*, *52*, 121–130.

Giglio, L., & Kendall, J. (2001). Application of the Dozier retrieval to wildfire characterization: A sensitivity analysis. *Remote Sensing of Environment*, *77*(1), 34–49.

Haines, D. (1988). A lower atmosphere severity index for wild-land fires. *National Weather Digest*, *13*(3), 23–27.

Holton, J., Haynes, P., McIntyre, M., Douglass, A., Rood, R., & Pfister, L. (1995). Stratosphere-troposphere exchange. *Reviews of Geophysics*, *33*(4), 403–439.

Hu, Y., Winker, D., Vaughan, M., Lin, B., Omar, A., Trepte, C., et al. (2009). CALIPSO/CALIOP cloud phase discrimination algorithm. *Journal of Atmospheric and Oceanic Technology*, *26*(11), 2293–2309.
Jensen, E., Lawson, P., Baker, B., Pilson, B., Mo, Q., Heymsfield, A., et al. (2009). On the importance of small ice crystals in tropical anvil cirrus. *Atmospheric Chemistry & Physics*, *9*(15), 5519–5537.
Jones, T., & Christopher, S. (2010). Satellite and radar observations of the 9 April 2009 Texas and Oklahoma grassfires. *Bulletin of the American Meteorological Society*, *91*(4), 455–460.
Khain, A., BenMoshe, N., & Pokrovsky, A. (2008). Factors determining the impact of aerosols on surface precipitation from clouds: An attempt at classification. *Journal of the Atmospheric Sciences*, *65*(6), 1721–1748.
Khain, A., Rosenfeld, D., & Pokrovsky, A. (2005). Aerosol impact on the dynamics and microphysics of deep convective clouds. *Quarterly Journal of the Royal Meteorological Society*, *131*(611), 2639–2663.
LaRoche, K., & Lang, T. (2017). Observations of ash, ice, and lightning within pyrocumulus clouds using polarimetric NEXRAD radars and the national lightning detection network. *Monthly Weather Review*, *145*(12), 4899–4910.
Lareau, N., & Clements, C. (2016). Environmental controls on pyrocumulus and pyrocumulonimbus initiation and development. *Atmospheric Chemistry and Physics*, *16*(6), 4005.
Lee, S., Donner, L., Phillips, V., & Ming, Y. (2008). The dependence of aerosol effects on clouds and precipitation on cloud-system organization, shear and stability. *Journal of Geophysical Research*, *113*, D16202. https://doi.org/10.1029/2007JD009224
Lindsey, D., & Fromm, M. (2008). Evidence of the cloud lifetime effect from wildfire-induced thunderstorms. *Geophysical Research Letters*, *35*, L22809. https://doi.org/10.1029/2008GL035680
Lindsey, D., Hillger, D., Grasso, L., Knaff, J., & Dostalek, J. (2006). GOES climatology and analysis of thunderstorms with enhanced 3.9-μm reflectivity. *Monthly Weather Review*, *134*(9), 2342–2353.
Lindsey, D., Miller, S., & Grasso, L. (2010). The impacts of the 9 April 2009 dust and smoke on convection. *Bulletin of the American Meteorological Society*, *91*(8), 991–996.
Livesey, N. J., Read, W. G., Wagner, P. A., Froidevaux, L., Lambert, A., Manney, G. L., et al. (2018). Version 4.2x level 2 data quality and description document, JPL D-33509 Rev. D.
Luderer, G., Trentmann, J., Winterrath, T., Textor, C., Herzog, M., Graf, H., & Andreae, M. (2006). Modeling of biomass smoke injection into the lower stratosphere by a large forest fire (part ii): Sensitivity studies. *Atmospheric Chemistry and Physics*, *6*(12), 5261–5277.
Melnikov, V., Zrnic, D., & Rabin, R. (2009). Polarimetric radar properties of smoke plumes: A model. *Journal of Geophysical Research*, *114*, D21204. https://doi.org/10.1029/2009JD012647
Mesinger, F., DiMego, G., Kalnay, E., Mitchell, K., Shafran, P., Ebisuzaki, W., et al. (2006). North American regional reanalysis. *Bulletin of the American Meteorological Society*, *87*(3), 343–360.
Miller, S., & Stephens, G. (2001). CloudSat instrument requirements as determined from ECMWF forecasts of global cloudiness. *Journal of Geophysical Research*, *106*(D16), 17713–17733. https://doi.org/10.1029/2000JD900645
Miller, S., Stephens, G., & Austin, R. (2001). GOES 10 cloud optical property retrievals in the context of vertically varying microphysics. *Journal of Geophysical Research*, *106*(D16), 17981–17995.
Mlawer, E., Taubman, S., Brown, P., Iacono, M., & Clough, S. (1997). Radiative transfer for inhomogeneous atmospheres: Rrtm, a validated correlated-k model for the longwave. *Journal of Geophysical Research*, *102*(D14), 16663–16682.
Peterson, D., Fromm, M., Solbrig, J., Hyer, E., Surratt, M., & Campbell, J. (2017). Detection and inventory of intense pyroconvection in western North America using GOES-15 daytime infrared data. *Journal of Applied Meteorology and Climatology*, *56*(2), 471–493.
Peterson, D., Hyer, E., Campbell, J., Fromm, M., Hair, J., Butler, C., & Fenn, M. (2015). The 2013 Rim Fire: Implications for predicting extreme fire spread, pyroconvection, and smoke emissions. *Bulletin of the American Meteorological Society*, *96*(2), 229–247.
Peterson, D., Hyer, E., Campbell, J., Solbrig, J., & Fromm, M. (2017). A conceptual model for development of intense pyrocumulonimbus in western North America. *Monthly Weather Review*, *145*(6), 2235–2255.
Potter, B. (2005). The role of released moisture in the atmospheric dynamics associated with wildland fires. *International Journal of Wildland Fire*, *14*(1), 77–84.
Prins, E., Feltz, J., Menzel, W., & Ward, D. (1998). An overview of GOES-8 diurnal fire and smoke results for SCAR-B and 1995 fire season in South America. *Journal of Geophysical Research*, *103*(D24), 31821–31835.
Pumphrey, H., Santee, M., Livesey, N., Schwartz, M., & Read, W. (2011). Microwave Limb Sounder observations of biomass-burning products from the Australian bush fires of February 2009. *Atmospheric Chemistry and Physics*, *11*(13), 6285–6296.
Reid, J., Koppmann, R., Eck, T., & Eleuterio, D. (2005). A review of biomass burning emissions part II: Intensive physical properties of biomass burning particles. *Atmospheric Chemistry and Physics*, *5*(3), 799–825.
Reutter, P., Trentmann, J., Seifert, A., Neis, P., Su, H., Chang, D., et al. (2014). 3-D model simulations of dynamical and microphysical interactions in pyroconvective clouds under idealized conditions. *Atmospheric Chemistry and Physics*, *14*(14), 7573–7583.
Rosenfeld, D., Fromm, M., Trentmann, J., Luderer, G., Andreae, M., & Servranckx, R. (2007). The Chisholm firestorm: Observed microstructure, precipitation and lightning activity of a pyro-cumulonimbus. *Atmospheric Chemistry and Physics*, *7*(3), 645–659.
Rosenfeld, D., Lohmann, U., Raga, G. B., O'Dowd, C. D., Kulmala, M., Fuzzi, S., et al. (2008). Flood or drought: How do aerosols affect precipitation? *Science*, *321*(5894), 1309–1313.
Rosenfeld, D., & Woodley, W. (2000). Deep convective clouds with sustained supercooled liquid water down to −37.5 °C. *Nature*, *405*(6785), 440.
Saleeby, S., & Cotton, W. (2008). A binned approach to cloud-droplet riming implemented in a bulk microphysics model. *Journal of Applied Meteorology and Climatology*, *47*(2), 694–703.
Schwartz, M., Read, W., Santee, M., Livesey, N., Froidevaux, L., Lambert, A., & Manney, G. (2013). Convectively injected water vapor in the North American summer lowermost stratosphere. *Geophysical Research Letters*, *40*, 2316–2321. https://doi.org/10.1002/grl.50421
Setvák, M., Lindsey, D., Novák, P., Wang, P., Radová, M., Kerkmann, J., et al. (2010). Satellite-observed cold-ring-shaped features atop deep convective clouds. *Atmospheric Research*, *97*(1-2), 80–96.
Sherwood, S. (2002a). A microphysical connection among biomass burning, cumulus clouds, and stratospheric moisture. *Science*, *295*, 1272–1275.
Sherwood, S. (2002b). Aerosols and ice particle size in tropical cumulonimbus. *Journal of Climate*, *15*(9), 1051–1063.
Simpson, J. (1980). Downdrafts as linkages in dynamic cumulus seeding effects. *Journal of Applied Meteorology*, *19*(4), 477–487.
Stein, A., Draxler, R., Rolph, G., Stunder, B., Cohen, M., & Ngan, F. (2015). NOAA's HYSPLIT atmospheric transport and dispersion modeling system. *Bulletin of the American Meteorological Society*, *96*(12), 2059–2077.
Stephens, G. L., Vane, D. G., Boain, R. J., Mace, G. G., Sassen, K., Wang, Z., et al. (2002). The CloudSat mission and the A-Train. *Bulletin of the American Meteorological Society*, *83*(12), 1771–1790. https://doi.org/10.1175/BAMS-83-12-1771

Trentmann, J., Luderer, G., Winterrath, T., Fromm, M., Servranckx, R., Textor, C., et al. (2006). Modeling of biomass smoke injection into the lower stratosphere by a large forest fire (part i): reference simulation. *Atmospheric Chemistry and Physics*, *6*(12), 5247–5260.

Uccellini, L., & Johnson, D. (1979). The coupling of upper and lower tropospheric jet streaks and implications for the development of severe convective storms. *Monthly Weather Review*, *107*(6), 682–703.

Walko, R., Cotton, W., Meyers, M., & Harrington, J. (1995). New RAMS cloud microphysics parameterization part I: The single-moment scheme. *Atmospheric Research*, *38*(1-4), 29–62.

Wang, P. (2003). Moisture plumes above thunderstorm anvils and their contributions to cross-tropopause transport of water vapor in midlatitudes. *Journal of Geophysical Research*, *108*(D6), 4194. https://doi.org/10.1029/2002JD002581

Wang, H., Skamarock, W., & Feingold, G. (2009). Evaluation of scalar advection schemes in the Advanced Research WRF model using large-eddy simulations of aerosol–cloud interactions. *Monthly Weather Review*, *137*(8), 2547–2558.

Weisman, M., & Klemp, J. (1982). The dependence of numerically simulated convective storms on vertical wind shear and buoyancy. *Monthly Weather Review*, *110*(6), 504–520.

Weisz, E., Li, J., Menzel, W., Heidinger, A., Kahn, B., & Liu, C. (2007). Comparison of AIRS, MODIS, CloudSat and CALIPSO cloud top height retrievals. *Geophysical Research Letters*, *34*, L17811. https://doi.org/10.1029/2007GL030676

Winker, D., Vaughan, M., Omar, A., Hu, Y., Powell, K., Liu, Z., et al. (2009). Overview of the CALIPSO mission and CALIOP data processing algorithms. *Journal of Atmospheric and Oceanic Technology*, *26*(11), 2310–2323. https://doi.org/10.1175/2009JTECHA1281.1